

DESIGN OF AN INSTRUMENT FOR SOIL MOISTURE AND ABOVE GROUND
BIOMASS REMOTE SENSING USING SIGNALS OF OPPORTUNITY

A Dissertation

Submitted to the Faculty

of

Purdue University

by

Benjamin R. Nold

In Partial Fulfillment of the

Requirements for the Degree

of

Master of Science in Electrical and Computer Engineering

August 2019

Purdue University

West Lafayette, Indiana

**THE PURDUE UNIVERSITY GRADUATE SCHOOL
STATEMENT OF DISSERTATION APPROVAL**

Dr. James Garrison, Co-Chair

School of Aeronautics and Astronautics

Dr. Mark Bell, Co-Chair

School of Electrical and Computer Engineering

Dr. Rajat Bindlish

NASA Goddard Space Flight Center

Approved by:

Dr. Dimitrios Peroulis

Head of the School Graduate Program

To my parents, Jonathan and Kimberly Nold

ACKNOWLEDGMENTS

I would like to thank my lab mates in no particular order: Abi, Jared, Han, Zenki, Aakash, Harris, Phillip, Feixion, and Katie. Thank you for pitching in and helping build the hardware, debug software, install the instrument on the trailer, swap data drives, and conduct science measurements in my absence. The field experiments would not have been successful without your help. I would also like to thank the undergraduate students that worked with me on the field experiments: Gabe, Kadir and Marvin. I'm very thankful for your assistance in the science collection, hardware assembly and tower maintenance.

I would also like to thank Manuel Vega, Jeff Piepmeier and Rajat Bindlish from Goddard Space Flight Center. The field experiments would not have been the success if it were not for your input on the experiment design, microwave hardware theory, practical engineering design advice and science expertise.

A big thank you goes out to Jim Beaty and the rest of the staff at Purdue ACRE. Your support was vital for the field experiment.

Lastly, I would like to thank my parents. I would have quit graduate school long before this thesis if it were not for the support from you. Thank you, Dad for the endless hours you spent with me discussing the mechanical design of the instrument. I must also thank you for taking the week in summer of 2018 to come help me assemble the tower; I doubt the tower would have ever been assembled if it was not for your help.

TABLE OF CONTENTS

	Page
LIST OF TABLES	viii
LIST OF FIGURES	ix
ABSTRACT	xii
1 INTRODUCTION	1
1.1 Ground Based Soil Measurement Techniques	2
1.2 Spaceborne Instruments	3
1.3 Signals of Opportunity	3
2 THEORETICAL DERIVATION	5
2.1 Electromagnetic Waves	5
2.1.1 Wave Polarization	6
2.1.2 Electromagnetic Wave-Media Interaction	7
2.1.3 Fresnel Zone	8
2.1.4 Specular Reflection	8
2.1.5 Penetration Depth	9
2.2 Signals of Opportunity Instrument	10
2.2.1 Reflectivity	11
2.2.2 Signal Ray Path Model	11
2.2.3 Correlation Operator	13
2.2.4 Noise Model	14
2.2.5 Signal Model	15
2.3 Calibration States	16
2.4 Reflectivity	20
3 INSTRUMENT DESIGN	22
3.1 Antennas	22

	Page
3.1.1 S-Band Antennas	22
3.1.2 P-Band Antennas	23
3.1.3 P-Band Antenna Ground Plane Mesh	24
3.1.4 P-Band Antenna Design Issues	25
3.2 RF Front End	27
3.2.1 S-Band	28
3.2.2 P-Band	29
3.2.3 Front End Swap States	29
3.2.4 Temperature Sensors	31
3.3 Link Budget	31
3.4 Equipment Shed	33
3.4.1 Phase Calibration Unit	34
3.4.2 Digital Receiver	34
3.4.3 Relay Controller	35
3.5 Data Management	35
4 FIELD EXPERIMENT	36
4.1 2017 Sensor Placement	37
4.1.1 Antenna Orientation	38
4.2 2018 Sensor Placement	38
4.2.1 Antenna Orientation	39
4.3 In Situ Truth Measurements	40
4.3.1 In Situ Soil Moisture Sensors	41
4.3.2 Gravimetric Soil Sampling	43
4.3.3 Theta Probe	43
4.3.4 Crop Measurements	44
4.3.5 Inferred Vegetation Measurements	44
5 IN SITU OBSERVATIONS	46
5.1 2017 Observations	46

	Page
5.1.1	Soil Moisture 46
5.1.2	Vegetation 46
5.2	2018 Observations 47
5.2.1	Gravimetric Soil Moisture 47
6	EXPERIMENT SUMMARY 53
6.1	Instrument Changes Summary 53
6.2	Timeline of Major Events - 2017 Experiment 53
6.3	Timeline of Major Events - 2018 Experiment 54
6.4	Validation of Microwave Data 55
6.4.1	P-Band 55
6.4.2	S-Band 59
6.5	Recommended Instrument Improvements 62
6.5.1	Microwave Hardware Improvements 62
6.5.2	In-situ instrument Improvements 63
6.5.3	Software Improvements 64
6.6	Conclusions 64
	REFERENCES 65
A	ANTENNA SIMULATIONS 67
B	MICROWAVE SCHEMATICS 75
C	SCIENCE MEASUREMENT SHEETS 77
D	FRONT END 2017 SCATTERING PLOTS 80
E	FRONT END 2018 SCATTERING PLOTS 84
F	FRONT END BILL OF MATERIAL 87

LIST OF TABLES

Table	Page
2.1 Rayleigh Criterion Values	9
2.2 Signal Properties	10
2.3 Model Parameters	15
3.1 Simulation Parameters	27
3.2 Front End Noise Figures	28
3.3 Front End States	30
3.4 Noise Temperatures for Antennas	33
3.5 Link Budget for Purdue SoOp Tower Experiment	33
3.6 Recording Data Rate	35
5.1 Plants per m^2 - 2018	51
6.1 Key instrument changes by year	53
6.2 2017 Campaign Timeline	53
6.3 2018 Campaign Timeline	54
6.4 Data Logger Dead Battery Events	54
F.1 Phase Calibration Bill of Material	88
F.2 Phase Calibration Bill of Material	89

LIST OF FIGURES

Figure	Page
1.1 The Water Cycle [3]	2
2.1 Signals of Opportunity Graphic	5
2.2 Cartesian Coordinates	6
2.3 Electromagnetic Wave Reflection	7
2.4 Ray Path Diagram	9
2.5 Soil Penetration Depth	10
2.6 Reflectivity Graphic	11
2.7 Ray Path Diagram	12
2.8 Through State	17
2.9 Swap State	18
2.10 Load State	19
2.11 Phase State	20
3.1 System Block Diagram	23
3.2 Antennas Mounted on Tower - 2017	24
3.3 P-Band Antenna Schematic	25
3.4 P-Band Antenna Schematic	25
3.5 P-Band Antenna Simulated 3D Gain Pattern	26
3.6 Damaged P-Band Antennas	26
3.7 Original Mesh	27
3.8 Improved Mesh	27
3.9 S-Band Microwave Block Diagram	29
3.10 P-Pand Microwave Block Diagram	30
3.11 2018 Front End Timing Diagram	31
3.12 2017 Front End Timing Diagram	31

Figure	Page
3.13 Phase Calibration Unit	34
4.1 2018 Field Experiment Tower Setup	36
4.2 2017 Experiment Map: In Situ Sensor Locations and Estimated Fresnel Zones	37
4.3 Sky Oriented Vertical P-Band Antenna	39
4.4 2017 Earth Vertical P-Band Antenna	39
4.5 2017 Tower Top View	39
4.6 2017 Tower Top View	39
4.7 2018 Experiment Map: In Situ Sensor Locations and Estimated Fresnel Zones	40
4.8 2018 Sky S-Band Antenna	41
4.9 2018 Earth S-Band Antennas	41
4.10 2018 Earth Vertical P-Band Antenna Orientation	41
4.11 2018 Earth Horizontal P-Band Antenna Orientation	41
4.12 2018 Tower Top View	42
4.13 2018 Tower Top View	42
4.14 HydraProbe Installation - 2018 Field Experiment	43
4.15 In Row Sampling Locations	44
5.1 2017 HydraProbe Soil Moisture	46
5.2 2017 Vegetation Water Content	47
5.3 Precipitation and HydraProbe Dielectric Readings - Half Tile Location	48
5.4 Precipitation and HydraProbe Dielectric Readings - On Tile Location	48
5.5 On Tile Soil Moisture Measurements	49
5.6 Quarter Tile Soil Moisture Measurements	49
5.7 Half Tile Soil Moisture Measurements	50
5.8 2018 Vegetation Water Content - Drainage Tile	51
5.9 2018 Vegetation Water Content - Quarter Tile	52
5.10 2018 Vegetation Water Content - Half Tile	52
6.1 MUOS Spectrum, Centered at 370 MHz - 6/29/18 14:00	56

Figure	Page
6.2 MUOS Ambiguity Functions - 6/29/18 14:00	57
6.3 MUOS Spectrum, Centered at 370 MHz - 6/29/18 14:15	57
6.4 MUOS Ambiguity Functions - 6/29/18 14:15	58
6.5 XM Spectrum, Centered at 2.344 GHz - 8/02/18 15:00	59
6.6 XM Ambiguity Functions - 8/02/18 15:00	60
6.7 XM Spectrum, Centered at 2.344 GHz - 8/02/18 15:15	60
6.8 XM Ambiguity Functions - 8/02/18 15:15	61
A.1 Gain Pattern with Antenna and Backplane	68
A.2 Feed Impedance at 370Mhz: $150.9365 -3.0728i \Omega$	68
A.3 Measured S11	69
A.4 Measured VSWR	70
A.5 Coax to Antenna Elements Soldering	73
A.6 P-Band Antenna Schematic	74
A.7 P-Band Antenna Schematic	74
B.1 2017 S-Band Front End Block Schematic	75
B.2 2018 S-Band Front End Block Schematic	75
B.3 2018 P-Band Front End Block Schematic	76
D.1 Network Analyzer Graphic	80
D.2 S21, 150Ft RG-8 cable, S-Band range	83
D.3 S21, 150Ft RG-8 cable, P-Band range	83
E.1 P-Band S21 measurements	85
E.2 2018 S-Band S21 Plots	86

ABSTRACT

Nold, Benjamin R. M.S.E., Purdue University, August 2019. Design of an Instrument for Soil Moisture and Above Ground Biomass Remote Sensing using Signals of Opportunity. Major Professor: James L. Garrison.

Measurements of soil moisture are a crucial component for understanding the global water and carbon cycle, weather forecasting, climate models, drought prediction, and agriculture production. Active and passive microwave radar instruments are currently in use for remote sensing of soil moisture. Signals of Opportunity (SoOp) based remote sensing has recently emerged as a complementary method for soil moisture remote sensing. SoOp reuses general digital communication signals allowing the reuse of allocated wireless communication signal bands for science measurements. This thesis developed a tower based SoOp instrument implementing frequencies in the P-Band and S-Band. Two field campaigns were conducted using this new instrument during the summers of 2017 and 2018 at Purdue's Agronomy Center for Research and Education.

1. INTRODUCTION

Knowledge of root-zone soil moisture is a vital component for weather forecasting, climate models, drought prediction, and agriculture. Soil moisture and above ground biomass have been identified by the World Meteorological Organization as an essential climate variable (ECV) for climate change studies [1]. Above ground biomass is a sink for atmospheric CO_2 by storing carbon in vegetation. It is also a source of carbon when biomass is combusted, such as wildfires and man-made fires. The National Oceanic and Atmospheric Administration (NOAA) estimates above ground biomass is a net sink for airborne carbon, removing approximately 20% of atmospheric CO_2 emissions from fossil fuels [2]. Above ground biomass also effects water quality and soil erosion [2]. Despite the importance in quantitatively measuring soil moisture and above ground biomass, current sensors are spatially restricted and temporally limited. Most of the current in situ sensors only provide a “pin dot” of spatial resolution. Even the current state-of-the-art remote sensing satellites only revisit a site on the order of a few days.

Soil moisture is a dominate factor in the radiation to land heat exchange, precipitation transitions to run-off water, and soil infiltration. On a spatially small scale, soil moisture controls above ground biomass growth [4]. The 2010 NASA Climate-Centric Architecture Plan identified that soil moisture data is crucial for predicting flood and droughts, agricultural production output predictions and climate change studies [5]. Temporally soil moisture measurements are important on an order of minutes for ground water runoff, to hours for depth penetration after a rain, to days for freeze-thaw and drought readings.

Measuring soil moisture on a global scale with ”sufficient” spatial and temporal resolution has provided many engineering challenges. Ground based in situ methods are “point scale” for spatial resolution [6]. An advantage to a spaceborne missions

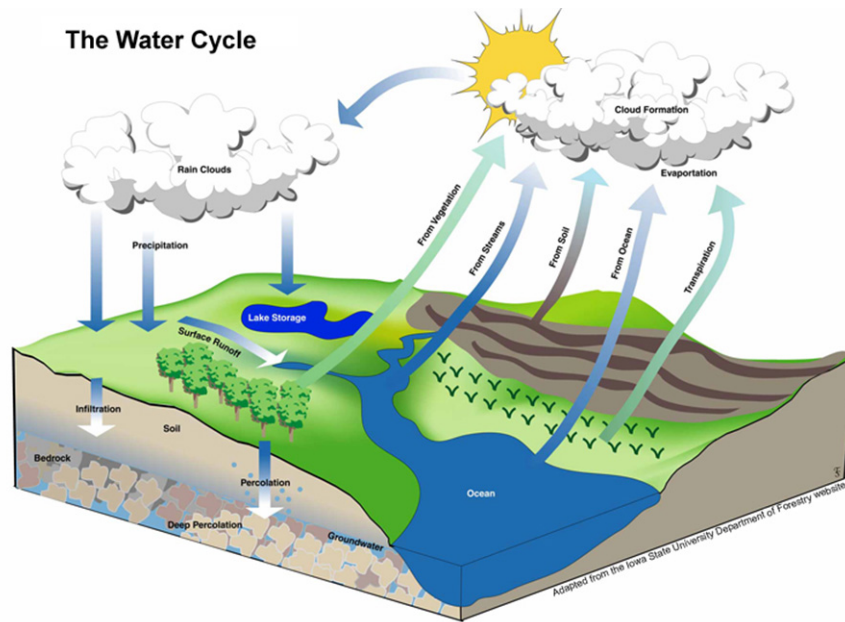


Fig. 1.1.: The Water Cycle [3]

is increased spatial resolution, typically with the cost of temporal resolution. The sensing depth of an instrument is also important, knowledge of root zone soil moisture (an order of 2 cm to 2 m) is essential for understanding the water recharge cycle. This thesis develops a tower based remote sensing instrument to estimate both soil moisture and above ground biomass.

1.1 Ground Based Soil Measurement Techniques

The gravimetric sampling method of measuring soil moisture requires a soil sample to be removed from the experiment site, weighed, placed in a soil oven to evaporate the moisture from the soil, then weighed again. Soil density must also be known, which is either estimated or experimentally determined. Gravimetric sampling is precise, but it only provides a “point measurement.” Multiple readings have to be made to obtain a representation of the experiment site. Temporally, the site has to be revisited for each measurement.

Electrical sensors have been developed to measure soil moisture based on a variety of techniques, including measuring capacitance, impedance, and time domain reflectivity of soil. These sensors require calibration for the specific experiment soil type and are buried at the location of interest in the experiment. Temporally these sensors can take measurements on sub-second intervals, but as with gravimetric sampling spatially these readings are “point measurements.”

1.2 Spaceborne Instruments

The SMAP mission is the current NASA spaceborne microwave instrument for sensing soil moisture. This space vehicle operates two microwave instruments in L-Band, a passive radiometer at 1.41 GHz and an active radar at 1.26 GHz. Spatially, SMAP has a 40 km diameter sensing footprint but temporally SMAP only revisits a measurement spot once every 3 days on average. SMAP operates in L-Band, therefore the soil penetration depth is limited to approximately 5 cm. Due to a work defect during assembly, the active radar failed on July 7, 2015, only the passive radiometer instrument is functioning [7], [8]. After the active radar failed on SMAP, the instrument was reconfigured to use GPS L2 as a GNSS-R instrument [9].

1.3 Signals of Opportunity

Recently, bi-static reflectometry using Signals of Opportunity (SoOp) has emerged as a new technology for remote sensing. This technique was first utilized for ocean winds applications using Global Navigation Satellite Systems (GNSS) as a source of illumination [10]. It was demonstrated in 2012 that any digital communication signals could be used as a source of illuminating for SoOp [11] [9]. This technology has been demonstrated in space with the launch of the Cyclone GNSS (CYGNSS) ocean winds sensing constellation.

Recent work focuses on using the data product from CyGNSS to estimate soil moisture. CyGNSS is designed to estimate ocean wind speed and direction via Delay

Doppler Maps (DDM), but the data product can be exploited to estimate soil moisture under certain conditions. Early work with CyGNSS's prototype instrument (TDS-1) determined that CyGNSS DDM's would only work for elevations below 3000 m [12]. It has been observed that CYGNSS does not provide accurate soil moisture estimation over sparsely or densely covered vegetation areas, limiting its overall usefulness as a soil moisture sensing instrument [13]. CYGNSS has also been used in conjunction with SMAP to augment the temporal resolution of the soil moisture data product.

SoOp instruments have been designed with the intention of estimating soil moisture. In 2002, a SoOp GNSS-based instrument was mounted on a fixed tower over a corn field. It was determined that the retrievals showed correlation with soil moisture in the top 1 cm of soil. It was observed that the reflection was quasi specular, and that vegetation and surface roughness negatively affected the measurement [14], [15]. After the active radar failed on SMAP, the instrument was reconfigured to use GPS L2 as a GNSS-R instrument [9].

An airborne instrument using Signals of Opportunity in both P-Band (240-270 MHz) and S-band (2.34 GHz) was developed and flown in 2016. The P-Band signal source had multiple channels with 5 kHz and 25 kHz bandwidths. Only a single 25 kHz channel was used in processing. The instrument showed a high reflectivity value over water as compared with land [16].

The instrument developed in this thesis uses one signal in P-Band (360-380 MHz) and another one S-Band (2.34 GHz). The P-Band signal is the Mobile User Operating System (MUOS), a U.S. government communication signal. The S-Band signal is SiriusXM Satellite Radio, a U.S. based nation-wide consumer radio. The instrument was mounted on a 106 ft. tall mobile antenna tower and two data campaigns were conducted, measuring bare soil and corn growth cycles.

2. THEORETICAL DERIVATION

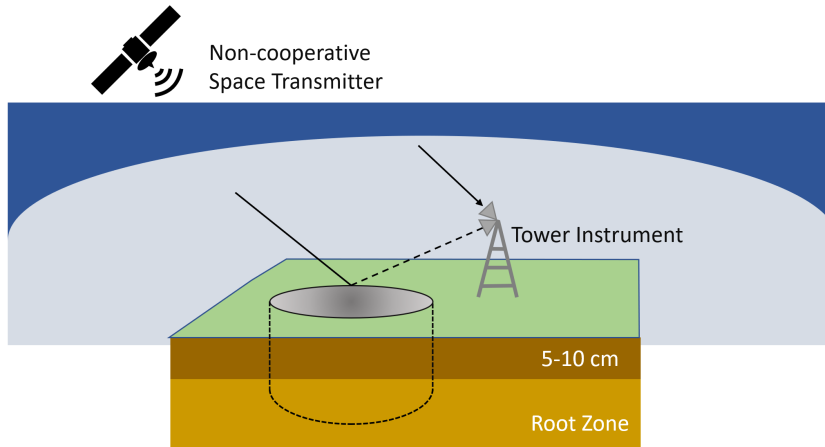


Fig. 2.1.: Signals of Opportunity Graphic

A Signals of Opportunity (SoOp) receiver is a passive instrument in a bi-static configuration. The illumination source is an existing, non-cooperative RF signal that is transmitted independently from the SoOp receiver. This allows remote sensing in RF bands allocated for digital communications. For soil moisture remote sensing, this allows the use of RF signals at frequencies below L-Band (the lowest allocated remote sensing band) for greater soil penetration depth.

2.1 Electromagnetic Waves

An electromagnetic wave can be modeled as a function of position and time. If an electric wave is propagating in the \hat{z} direction and oriented in the \hat{x} direction then it can be represented as:

$$\mathbf{E} = \hat{x}E_x(z, t) \quad (2.1)$$

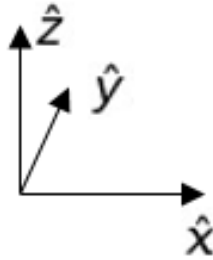


Fig. 2.2.: Cartesian Coordinates

2.1.1 Wave Polarization

An electromagnetic wave may be polarized into either a linear, elliptical or circular polarization. Due to the gyrotropic dielectric of the ionosphere, linearly polarized electromagnetic waves will become elliptically polarized while propagating through the ionosphere. If linear polarized waves are used for communication through the atmosphere, the receiver will measure an attenuated signal due to the Faraday rotation induced by the ionosphere. To overcome this, satellite communication signals are commonly elliptically or circularly polarized.

Wave polarization can be represented as:

$$\mathbf{E} = \hat{x}E_x(z, t) + \hat{y}E_y(z, t) \quad (2.2)$$

$$E_x(z, t) = E_1 \cos(\omega t - \beta z) \quad (2.3)$$

$$E_y(z, t) = E_2 \cos(\omega t - \beta z + \alpha) \quad (2.4)$$

If $\alpha = +\frac{\pi}{2}$, then the wave is Left Hand Circular Polarized (LHCP) and if $\alpha = -\frac{\pi}{2}$ then the wave is Right Hand Circular Polarized (RHCP). The wave is linearly polarized if E_x or E_y is zero.

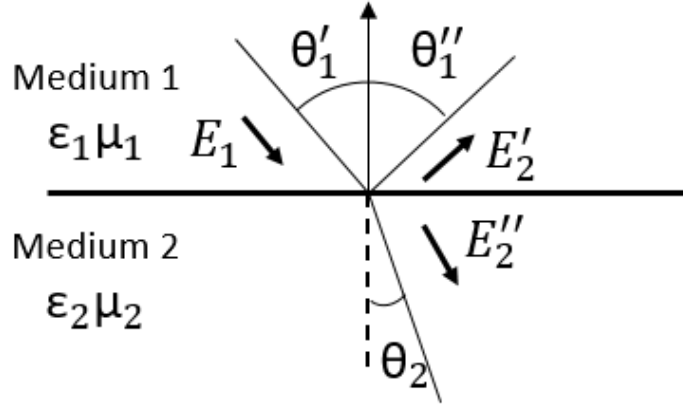


Fig. 2.3.: Electromagnetic Wave Reflection

2.1.2 Electromagnetic Wave-Media Interaction

When an electromagnetic wave transitions between two media the wave may split, partially reflecting and transmitting. The Fresnel coefficients determine the amplitude of the reflected and transmitted wave due to the differences in permittivity between the media. The Fresnel coefficient for a horizontally-polarized plane wave is given by:

$$R_{hh} = \frac{E''_{H1}}{E'_{H1}} = \frac{\cos(\theta_1) - \sqrt{\epsilon_{2r} - \sin^2(\theta_1)}}{\cos(\theta_1) + \sqrt{\epsilon_{1r} - \sin^2(\theta_1)}} \quad (2.5)$$

where: $\epsilon_{1r}, \epsilon_{2r}$ are the complex dielectric constants of the media.

Similarly for a vertically polarized plane wave:

$$R_{vv} = \frac{E''_{V1}}{E'_{V1}} = \frac{\epsilon_{2r}\cos(\theta_1) - \sqrt{\epsilon_{2r} - \sin^2(\theta_1)}}{\epsilon_{2r}\cos(\theta_1) + \sqrt{\epsilon_{2r} - \sin^2(\theta_1)}} \quad (2.6)$$

A simpler transformation can be done to convert from horizontally polarized waves to circular polarization.

$$\begin{bmatrix} R_{rr} & R_{rl} \\ R_{lr} & R_{ll} \end{bmatrix} = \frac{1}{2} \begin{bmatrix} R_{hh} + R_{vv} & R_{hh} - R_{vv} \\ R_{hh} - R_{vv} & R_{hh} + R_{vv} \end{bmatrix}$$

Where the subscripts h and v denote horizontal and vertical polarization. The subscripts rr and ll correspond to the wave that remains RHCP or LHCP upon

reflection. The subscripts rl and lr correspond to the wave that changes from RHCP to LHCP upon reflection and LCHP to RHCP respectively.

2.1.3 Fresnel Zone

The footprint size of the reflection zone is derived from the Fresnel zone. The Fresnel zone as shown in Figure 2.4 is an ellipsoid with semi-minor axis is given as:

$$b = \sqrt{n\lambda \frac{D_{TS}D_{RS}}{D_{TS} + D_{RS}}} \quad (2.7)$$

where n is the Fresnel Zone Number, λ is the wavelength, D_{TS} is the distance between the transmitter and the specular point, D_{RS} is the distance between the receiver and the specular point. It can be simplified to:

$$b \approx \sqrt{n\lambda D_{RS}} \approx \sqrt{\frac{\lambda h}{\sin(\theta)}} \quad (2.8)$$

$$a = \frac{b}{\sin(\theta)} \quad (2.9)$$

where h is the height of the receiver and θ is the elevation of the transmitter.

2.1.4 Specular Reflection

A wave reflection is considered to be specular if there is a single reflected wave from the reflection point. Consider a flat, semi-infinite surface defining the interface between a medium and air. Due to the Rayleigh criterion, as long as the phase difference between two reflected waves is less than $\frac{\pi}{2}$ radians then the reflection may be considered to be specular. More formally, the Rayleigh criterion is defined as:

$$\sigma_z \leq \frac{\lambda}{8\cos\theta} \quad (2.10)$$

Where σ_z is the standard deviation of the surface height of the reflection point. Values for the signals used in this instrument are displayed in Table 2.1

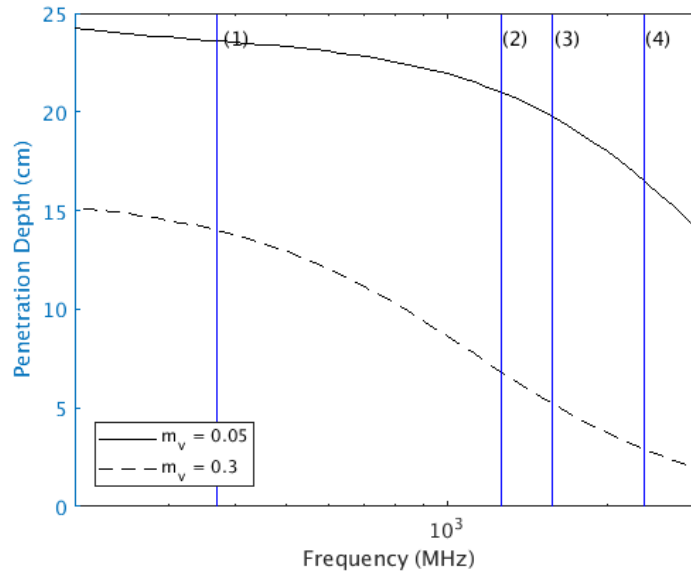


Fig. 2.5.: Soil Penetration Depth

2.2 Signals of Opportunity Instrument

Two SoOp sources were chosen to be used by this instrument: the Mobile User Objective System (MUOS) in P-Band and SiriusXM Radio in S-Band. Both transmitter are geostationary, simplifying experiment design.

Table 2.2.: Signal Properties

Signal Band	P-Band	S-Band
Transmitter Name	MUOS	XM
Frequency	370 MHz	2.34 GHz
Channels	4	2
Channel Bandwidth	5 MHz	1.64 MHz
Total Available Bandwidth	20 MHz	1.64 MHz

2.2.1 Reflectivity

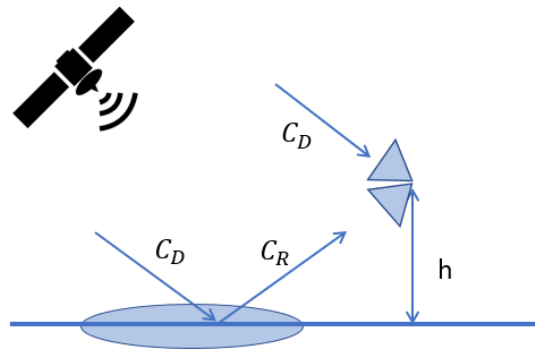


Fig. 2.6.: Reflectivity Graphic

A SoOp instrument measures effective reflection coefficient \mathcal{R}_{eff} from which the true reflectivity Γ is estimated. Reflectivity Γ is determined by the interference of the electromagnetic source of illumination's interaction with the media of interest. It is defined as the ratio of “reflected” (C_R) to incident or “direct” (C_D) power:

$$\Gamma = \frac{C_R}{C_D} \quad (2.11)$$

2.2.2 Signal Ray Path Model

A ray path model is as follows for Signals of Opportunity. In this setup the SoOp receiver consists of two antennas (sky, earth), fixed at a height above the reflection point. Both the transmitter and receiver are stationary. The following assumptions are made:

1. The distance between the transmitter and receiving antennas is infinity.
 - This assumption allows us to assume the angle of incident for C_D at the antenna and the reflection point are the same while ignoring the propagation losses due the additional path length.

- This allows us to approximate signal power from the transmitter at the reflection point as equal to that of direct antenna.
2. There is perfect isolation between the sky and earth antenna.
 3. The reflection is specular

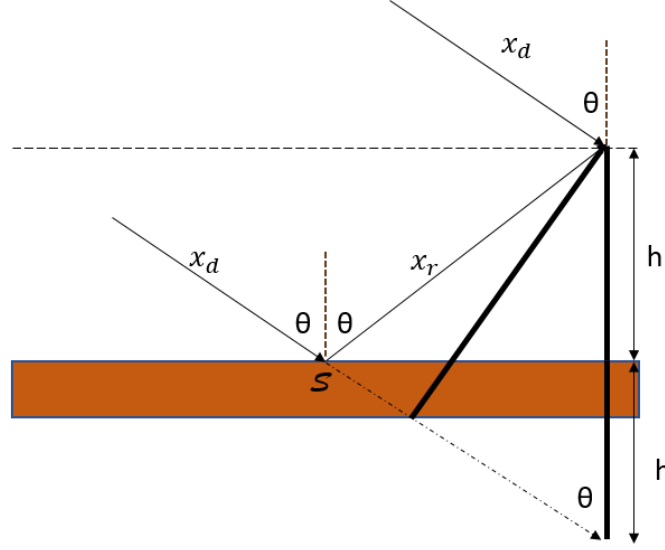


Fig. 2.7.: Ray Path Diagram

The transmitted signal with transmit power C , modulation $s(t)$ and carrier $e^{j\omega ct}$ can be modeled as:

$$x_T(t) = \sqrt{C}s(t)e^{j\omega ct} \quad (2.12)$$

The direct signal at the sky antenna:

$$x_D(t) = \sqrt{C_D}s(t - \tau_D)e^{j\omega(t - \tau_D)} \quad (2.13)$$

Similarly for the reflected signal at the earth antenna:

$$x_R(t) = \sqrt{C_R}s(t - \tau_R)e^{j\omega(t - \tau_R)} \quad (2.14)$$

Where τ_D is the estimated time delay between the transmitter and the sky antenna. τ_R is the estimated time delay between the transmitter and the earth antenna

(include the time from the reflection point to the earth antenna). Under the assumption that the distance between transmitter and receiver is infinity, the direct and reflected ray paths are approximately parallel. The spacial distance between the direct and reflected signal paths d is:

$$d = 2h\cos(\theta) \quad (2.15)$$

Where θ is the angle of incidence, and d is related to the time difference between the direct and reflected path via:

$$\tau_R - \tau_D = \Delta\tau = \frac{2h\cos(\theta)}{c} = \frac{d}{c} \quad (2.16)$$

where c is the speed of light.

2.2.3 Correlation Operator

A receiver computes an approximation of a correlation between two signals as:

$$R_{12}(\tau) = \int_{T_I} x_1(t)x_2^*(t - \tau)dt \quad (2.17)$$

The autocorrelation is correlation of the time series with itself:

$$R_{11}(\tau) = \int_{T_I} x_1(t)x_1^*(t - \tau)dt \quad (2.18)$$

A communication signal is a power signal, where the average power is approximated (for long T_I) as:

$$P_x = \frac{1}{T_I} \int_{T_I} |x(t)|^2 dt \quad (2.19)$$

Evaluating the auto-correlation at $\tau = 0$ is proportional to the signal's average power:

$$P_x = R_{11}(0) = \frac{1}{T_I} \int_{T_I} x_1(t)x_1^*(t)dt \quad (2.20)$$

The normalization factor $\frac{1}{T_I}$ is to set the dimensions in terms of power.

2.2.4 Noise Model

This signal model will only consider thermal noise from the amplifiers and antennas. It is assumed that there is not a common source of noise present in both receiver channels. Thermal noise is additive white Gaussian noise with a power spectral density of:

$$S(f) = \frac{N_0}{2} \quad (2.21)$$

The microwave front end applies an anti-aliasing filter of bandwidth B to the noise. The filter has a frequency response approximated by:

$$H(f) = \begin{cases} 1, & |f| \leq B \\ 0, & |f| > B \end{cases}$$

After filtering the Power Spectral Density is then:

$$S_\eta(f) = \begin{cases} \frac{N_0}{2}, & |f| \leq B \\ 0, & |f| > B \end{cases}$$

The noise power of $\eta(t)$ is then:

$$P_n = \int_{-\infty}^{\infty} S_n(f) df = \frac{N_0}{2} \int_{-B}^B 1 dF = N_0 B \quad (2.22)$$

The thermal noise power is $P = kTB$, where k is Boltzmann's constant, T_e is the equivalent noise temperature in Kelvin, and B is the bandwidth.

The auto-correlation function of P_n :

$$R_n(\tau) = \mathcal{F}^{-1}\{S_\eta\} = \int_{-B}^B \frac{N_0}{2} e^{j2\pi f\tau} = N_0 \frac{\sin(2\pi B\tau)}{2\pi\tau} = N_0 B \text{sinc}(2B\tau) \quad (2.23)$$

$$\text{sinc}(2\pi B\tau) = \begin{cases} 1 - \left| \frac{\sin(2B\tau)}{2\pi B\tau} \right|, & \tau \leq \frac{1}{2B} \\ \approx 0, & \tau \geq \frac{1}{2B} \end{cases}$$

η then follows:

$$E\{\eta\} = 0 \quad (2.24)$$

$$R_{12}(\tau) = E\{\eta_1(t), \eta_1^*(t - \tau)\} = N_0 B \text{sinc}(2\pi B\tau) \quad (2.25)$$

$$E\{\eta_1(t)\eta_2^*(t - \tau)\} \approx 0 \quad (2.26)$$

$E\{\eta\}$ is the expected value operator.

2.2.5 Signal Model

Table 2.3.: Model Parameters

Name	Symbol
Amplifier Gain of RF System 1	G_1
Amplifier Gain of RF System 2	G_2
Sky Antenna Gain	$G_{A,S}$
Earth Antenna Gain	$G_{E,S}$
System 1 Noise	η_1
System 2 Noise	η_2
Reflectivity	Γ
Sky Antenna Brightness Temperature	$\eta_{A,S}$
Earth Antenna Brightness Temperature	$\eta_{A,E}$
Matched Load Noise	η_{ref}

All sources of noise in a microwave system can be converted into an equivalent noise temperature T_e . A matched load has a noise temperature equal to the devices physical temperature. The noise temperature of the sky and earth antennas, represented by $\eta_{A,S}$ and $\eta_{A,E}$, can be determined using the method developed in Section 3.3.

The digital receiver has two inputs A and B and it performs the down conversion to baseband before the Analog to Digital (A to D) conversion. The signal as received by the digital receiver after down conversion in inputs A and B is modeled as:

$$x_A(t) = \sqrt{G_1}(\sqrt{G_{A,S}}x_D(t) + \eta_1(t)) \quad (2.27)$$

$$x_B(t) = \sqrt{G_2}(\sqrt{G_{A,E}}x_R(t) + \eta_2(t)) \quad (2.28)$$

Computing the auto-correlation of the received signals, for channel A:

$$R_{AA}(\tau) = G_1 \left(G_{A,S} C_D R_S(\tau) + (T_{A,S} + T_1) k B \text{sinc}(2B\tau) \right) \quad (2.29)$$

Similarly for channel B:

$$R_{BB}(\tau) = G_2 \left(G_{A,E} C_R R_S(\tau) + (T_{A,E} + T_2) k B \text{sinc}(2B\tau) \right) \quad (2.30)$$

The cross correlation between channels A and B:

$$R_{AB}(\tau) = \sqrt{G_1 G_2 C_D C_R G_{A,S} G_{A,E}} \left(R_S(\tau - \tau_{RD}) \right) \quad (2.31)$$

The random variables η_1 and η_2 are independent processes. The time difference:

$$\tau_{RD} = \tau_R - \tau_D.$$

2.3 Calibration States

The microwave RF system will have wide band thermal noise from the environment and amplifiers. The front end was designed with 4 states for system calibration: through, swap, load and phase. B is the bandwidth of the RF anti-aliasing filters in the digital receiver. The signals $x_A(t)$, $x_B(t)$ correspond to inputs A and B of the digital receiver after down conversion to baseband.

Through

$$x_A(t) = \sqrt{G_1}(\sqrt{G_{A,S}}x_D(t) + \eta_{A,S}(t) + \eta_1(t)) \quad (2.32)$$

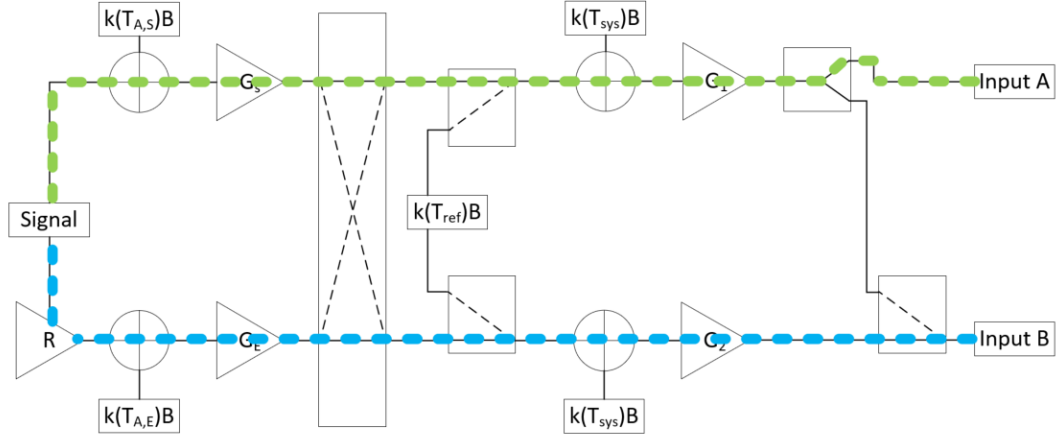


Fig. 2.8.: Through State

$$x_B(t) = \sqrt{G_2}(\sqrt{G_{A,E}}x_R(t) + \eta_{A,E}(t) + \eta_2(t)) \quad (2.33)$$

$$R_{AA}^t(\tau) = G_1 \left(G_{A,S} C_D R_S(\tau) + (T_{A,S} + T_1) k B \text{sinc}(2B\tau) \right) \quad (2.34)$$

$$R_{BB}^t(\tau) = G_2 \left(G_{A,E} C_D \Gamma R_S(\tau) + (T_{A,E} + T_2) k B \text{sinc}(2B\tau) \right) \quad (2.35)$$

$$R_{AB}^t = C_D \sqrt{G_1 G_2 G_{A,S} G_{A,E} \Gamma} (R_S(\tau - \tau_{RD})) \quad (2.36)$$

Swap

The transfer switch is used to swap the amplifiers between the Sky and Earth Antenna.

$$x_A(t) = \sqrt{G_1}(\sqrt{G_{A,E}}x_R(t) + \eta_{A,E}(t) + \eta_1(t)) \quad (2.37)$$

$$x_B(t) = \sqrt{G_2}(\sqrt{G_{A,S}}x_D(t) + \eta_{A,S}(t) + \eta_2(t)) \quad (2.38)$$

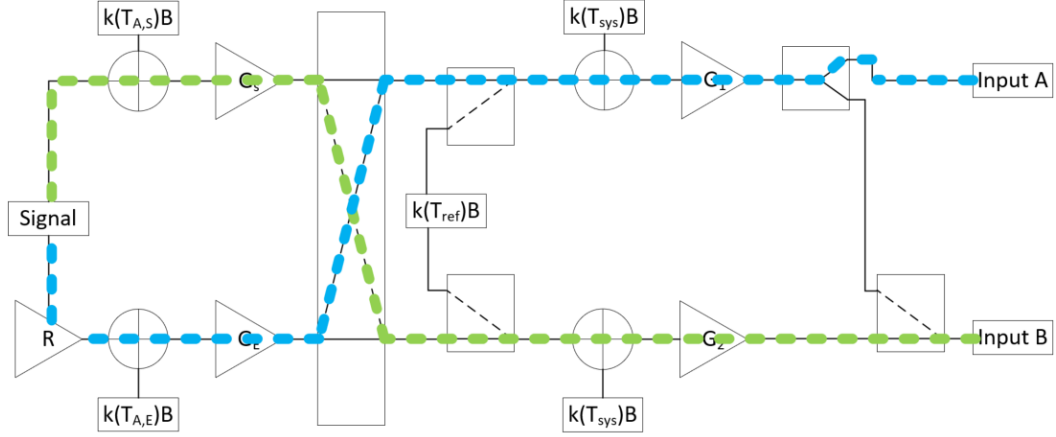


Fig. 2.9.: Swap State

$$R_{AA}^s(\tau) = G_1 \left(G_{A,E} C_D \Gamma R_S(\tau) + (T_{A,E} + T_1) k B \text{sinc}(2B\tau) \right) \quad (2.39)$$

$$R_{BB}^s(\tau) = G_2 \left(G_{A,S} C_D R_S(\tau) + (T_{A,S} + T_2) k B \text{sinc}(2B\tau) \right) \quad (2.40)$$

$$R_{AB}^s = C_D \sqrt{G_1 G_2 G_{A,S} G_{A,E} \Gamma} (R_S(\tau - \tau_{RD})) \quad (2.41)$$

Load

Reflective switches were used to switch in matched loads into the receiver chains. The noise sources η_{ref} are generated by separate matched loads, η_{ref} in each receiver chain and are uncorrelated. In each amplifier T_{ref} is the temperature of the matched load which was recorded with a Resistance Temperature Detector RTD temperature sensor. The η_{ref} are independent noise sources in channel A and B. However, the match loads have the same noise power as they were both the same temperature (connected via copper tape).

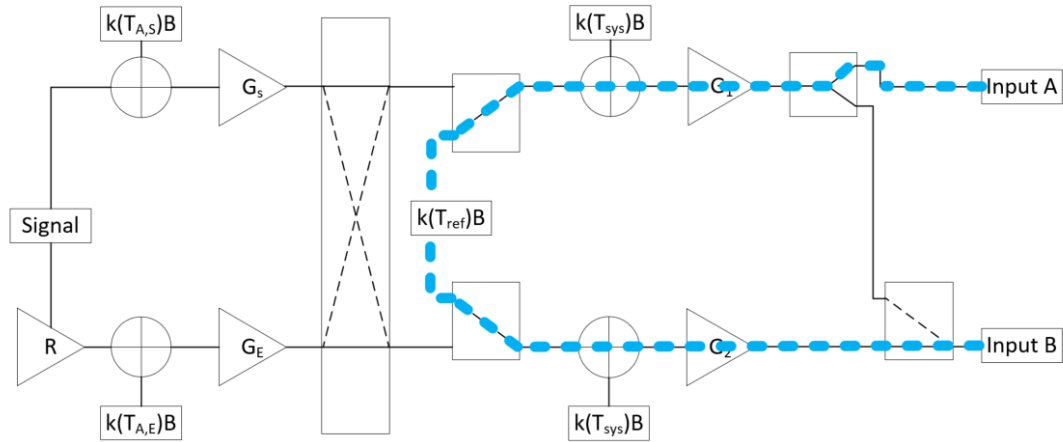


Fig. 2.10.: Load State

$$x_A(t) = \sqrt{G_1} \left(\eta_{ref}(t) + \eta_1(t) \right) \quad (2.42)$$

$$x_B(t) = \sqrt{G_2} \left(\eta_{ref}(t) + \eta_2(t) \right) \quad (2.43)$$

$$R_{AA}^l(\tau) = G_1 \left((T_{ref} + T_1) k B \text{sinc}(2B\tau) \right) \quad (2.44)$$

$$R_{BB}^l(\tau) = G_2 \left((T_{ref} + T_1) k B \text{sinc}(2B\tau) \right) \quad (2.45)$$

$$R_{AB}^l(\tau) = 0 \quad (2.46)$$

Phase

A reflective switch was used to connect the sky antenna and amplifier chain into both inputs. This was added to verify that the phase of the two input channels of the digital receiver were phase synchronized.

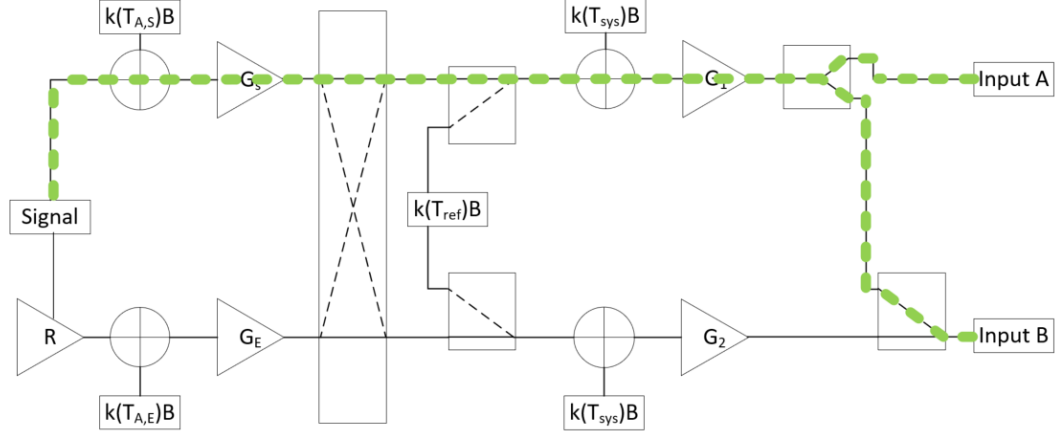


Fig. 2.11.: Phase State

$$x_A(t) = \sqrt{G_1} \left(\sqrt{G_{A,S} C_D} x_D(t) + \eta_1 \right) \quad (2.47)$$

$$x_B(t) = \sqrt{G_1} \left(\sqrt{G_{A,S} C_D} x_D(t) + \eta_1 \right) \quad (2.48)$$

If $x_A(t)$ and $x_B(t)$ are phased synchronized, then:

$$R_{AB}^l(\tau) = G_1 \left(G_{A,S} C_D R_S(\tau) + (T_{A,S} + T_1) k B \text{sinc}(2B\tau) \right) \quad (2.49)$$

2.4 Reflectivity

We make the assumption that the reflection coefficient measured by the digital receiver \mathcal{R}_{eff} is approximately equal to the true reflectivity due to the short distance between the specular point and the receiver. \mathcal{R}_{eff} is proportional to the square root of the surface reflectivity Γ .

$$\mathcal{R}_{eff} = \sqrt{\frac{\Gamma G_1}{G_2}} \frac{\langle x_D(t) x_R^*(t - \tau_{RD}) \rangle}{\langle x_D(t) x_D^*(t) \rangle - (G_{A,S} k T_{A,S} B + \sigma_1^2)} \quad (2.50)$$

G_1/G_2 is found from the ratio of the auto-correlations of the direct and reflected channel when the front-end is switched to the load calibration state. In this mode, the antennas are disconnected $x_D(t)$ and $x_R(t)$ are both uncorrelated noise with equal variance due to the noise sources being held at the same temperature, such that

$$\frac{G_1}{G_2} = \frac{R_{R,C}(0)}{R_{D,C}(0)} \quad (2.51)$$

in which $R_{11}^l(0)$ and $R_{22}^l(0)$ are the autocorrelations computed from the load state.

3. INSTRUMENT DESIGN

For both the 2017 and the 2018 experiment, the instrument recorded digital communication signals in the P-band (370 MHz) and S-band (2.34 GHz) ranges. The instrument was designed to be installed on a 32 m tall mobile antenna tower trailer. The antennas and the corresponding RF front ends were installed on the top of the tower. One hundred fifty foot long power, digital communication, and RF signals (coax) cables were used to connect the front end to the digital receivers on the ground. All power and digital communication cables were double shielded to mitigate electromagnetic interference. The front end was installed inside of an aluminum box that was grounded to the tower's frame. The communication and power cable shielding were grounded to the front end and to the equipment shed at the bottom of the tower.

A system level block diagram of the instrument is shown in Figure 3.1. The 2017 and 2018 instruments were nearly the same, except the 2017 instrument only had a single earth polarization antenna. The 2018 instrument added the second polarization as shown by the blue lines. A complete summary of instrument changes is discussed in Section 6.

3.1 Antennas

3.1.1 S-Band Antennas

Off-the-shelf commercial XM radio passive patch antennas were used for S-Band. Satcom 2M23P-XS-2 antennas were used for the sky (RHCP signal) and earth signals respectively. For the 2017 field experiment, only a RHCP antenna was used for the

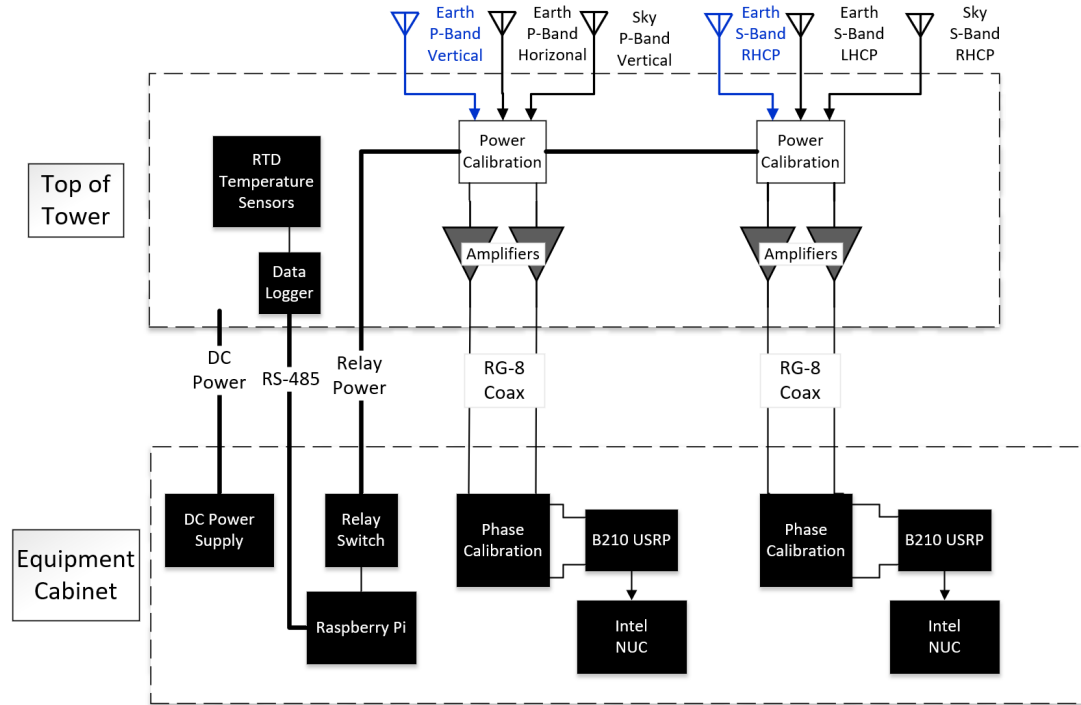


Fig. 3.1.: System Block Diagram

earth antenna. In 2018, an RHCP and LHCP antennas were used to record both reflection polarization.

In 2017, the S-Band antennas were mounted on 2ft x 4ft wide aluminum plates reused from an earlier experiment. Figure 3.2 shows the P-Band and S-Band antennas mounted on the trailer. In 2018 the S-Band antennas were placed on two smaller aluminum plates as shown in Figures 4.8, 4.9.

3.1.2 P-Band Antennas

Dipole antennas were designed and fabricated for the P-Band signal. The design featured nylon fasteners and acrylic mounting hardware to mitigate interference with the antenna gain pattern. The dipole element lengths were $0.95 * \lambda/2$ m long. A bazooka balun was used to match impedance between the antenna and the 50Ω coax.



Fig. 3.2.: Antennas Mounted on Tower - 2017

A ground plane approximately 1 wavelength square was positioned 0.25 wavelengths behind the dipole to increase the antenna's front-to-back ratio. Basic drawings are shown in Figures 3.3 and 3.4. OpenEMS was used to simulate the antenna and the simulated gain pattern is shown in Figure 3.5 [18]. Full simulation results are included in Appendix A. RG-58 was used to connect these antennas to the front end. Antenna drawings are also provided in the Appendix.

3.1.3 P-Band Antenna Ground Plane Mesh

Originally the ground plane mesh was a material used for window screens, as shown in Figure 3.7. It was observed that the wind could be audibly heard “whistling” through the mesh material when the tower was raised in 2017. The severe rain and windstorm on 7/11/2017 bent the ground plane frames as shown in Figure 3.6. The screen door mesh was replaced with a chicken wire mesh to reduce the wind drag as shown in Figure 3.8.

P-Band Dipole Antenna – not to scale

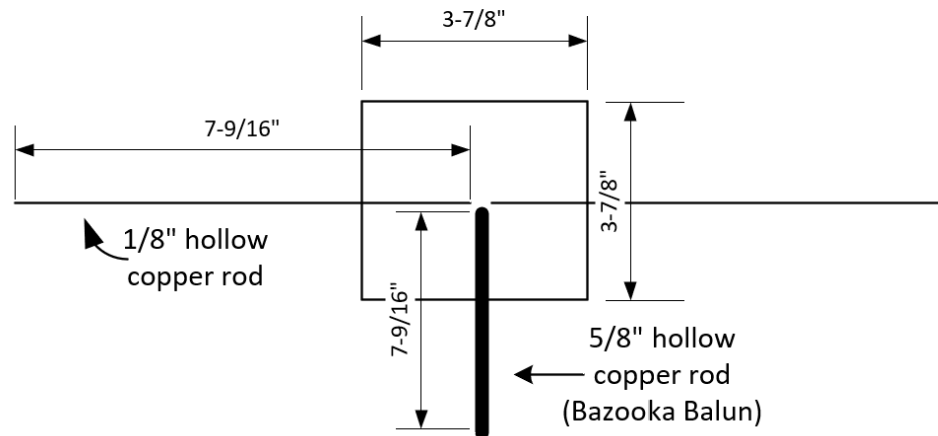


Fig. 3.3.: P-Band Antenna Schematic

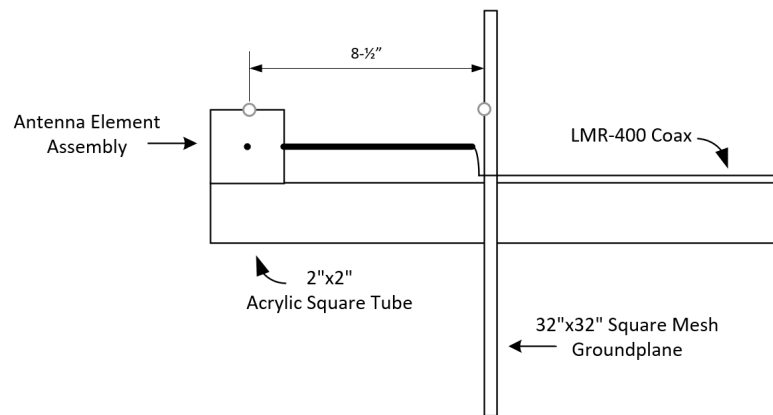


Fig. 3.4.: P-Band Antenna Schematic

3.1.4 P-Band Antenna Design Issues

The P-Band antennas were designed before the Radio Navigation Lab acquired a network analyzer with a calibration kit. It is observed from the simulations that the P-Band dipole antenna actually resonates at 301.6 MHz with the addition of the back plane. Using a network analyzer, S11 shows the antennas resonate at 322 MHz with a measured impedance of $26 - j19.1 \Omega$ and a VSWR is 2.282. Table 3.1 contains the

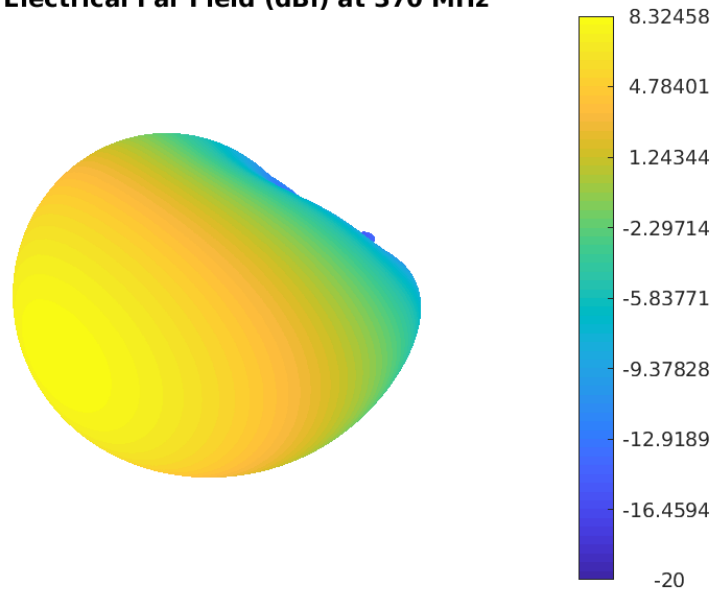
3D - Electrical Far Field (dBi) at 370 MHz

Fig. 3.5.: P-Band Antenna Simulated 3D Gain Pattern



Fig. 3.6.: Damaged P-Band Antennas



Fig. 3.7.: Original Mesh



Fig. 3.8.: Improved Mesh

Table 3.1.: Simulation Parameters

Name	370 Mhz Simulated	370 MHz Measured	Units
Feed Impedance	150 + 105.13i	26-19.1i	Ohms
VSWR	4.597	2.3	unitless

different antenna parameters for the resonate frequency of 301.6 MHz and the desired center frequency of 370 MHz using the results of the antenna simulation. Appendix A contains plots from the simulation using the center frequency of 370 MHz as well as the measured S11 plots obtained using the network analyzer.

3.2 RF Front End

The front end was installed in a waterproof aluminum washdown enclosure on the top of the tower, near the antennas. The box served to provide a shield for electrical interference as well as protect the electrical components from the weather.

The P-Band and S-Band system share a similar front end design, the primary differences being the amplifiers. The front end block diagrams are shown in Figures

3.9 and 3.10. The 2017 experiment the front end only had the capability to record a single earth antenna polarization for both P and S-Band. In 2018, two reflected (earth) antennas were used for both signals to record dual reflected polarizations.

The first stage of the front end consisted of a gas discharge tube lighting suppressor. The digital receiver input was time-multiplex using a reflective RF switch. A transfer switch was used to perform antenna swapping between the direct and reflected front end paths. Each signal was independently filtered and amplified, a standard SMA-SMA bulkhead connector was used to connect the front end chain to the coax cable.

Table 3.2.: Front End Noise Figures

Microwave Chain	Noise Figure [dB]	Noise Temperature [K]	Gain [dB]
2017 S-Band	3.12	283.35	69.8
2017 P-Band	3.37	316.51	46.8
2018 S-Band	0.91	62.67	76.93
2018 P-Band (before failure)	0.82	56.13	61.66

3.2.1 S-Band

No RF filters were installed in the S-Band front end chain. The system relied on the anti-aliasing filters in the USRP. In 2017, Mini-Circuits ZX60-2534M-S+ amplifiers were used and in 2018 Mini-Circuits ZX60-P103LN+ and ZX60-242GLN-S+ amplifiers were used to reduce the noise figure of the system. Detailed schematics are included in Appendix B. Table 3.2 contains the noise figure calculations for both experiment years.

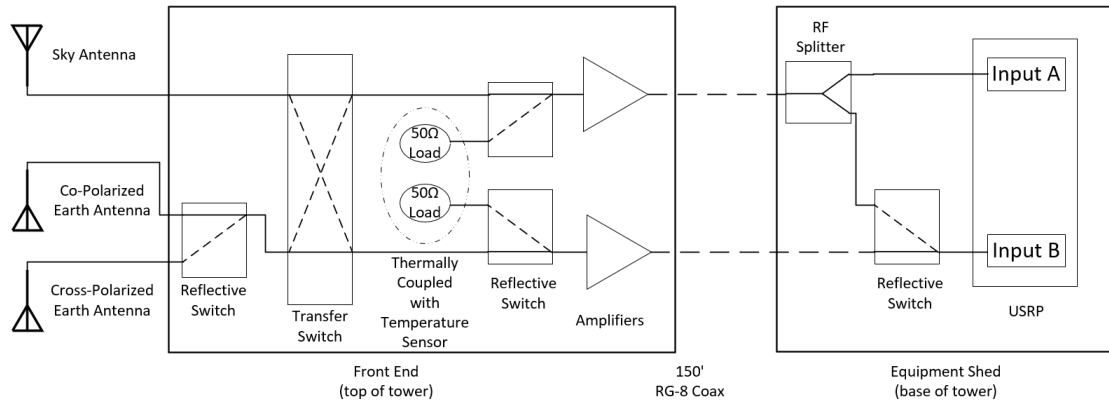


Fig. 3.9.: S-Band Microwave Block Diagram

3.2.2 P-Band

Both the 2017 and 2018 P-Band microwave systems used 2 sets of VLF-320+ and SHP-300+ filters. These filters were added to suppress any out of band RF frequencies. The full characteristics can be seen in Chapter E, Figure E.1.

Both experiment years used the ZRL-400+ amplifier. Note, the beginning of 2018 the P-Band system also included ZX60-P103LN+ amplifiers in the same configuration as the 2018 S-Band receiver, but for an unknown reason, the amplifiers failed. They were removed and the experiment continued only using the ZRL-400+. A full summary of the recording events, including the date the amplifiers failed and the front end was modified, is included in the Appendix 6.

3.2.3 Front End Swap States

For calibration purposes, the front end contained reflective and transfer switches to swap in a load, switch antennas for the alternate reflected polarization and to swap the antennas between the sky and earth amplifier/filter chains. The state swapping follows a defined sequence, encoding the current state in the length of time spent

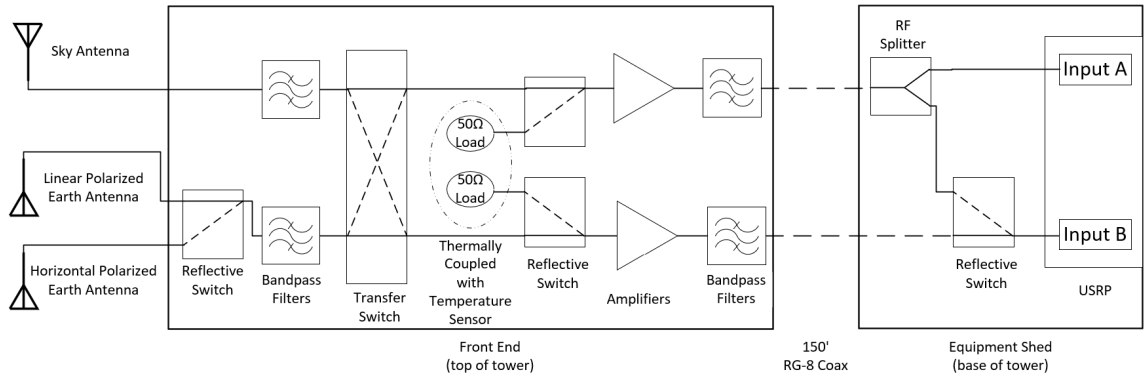


Fig. 3.10.: P-Pand Microwave Block Diagram

on the state. The sequence was asynchronous to the digital RF recording being controlled by the Raspberry Pi. The state information was not captured or saved with the RF data. Determining the state of the microwave front end was determined in post processing from the digital RF data. Table 3.3 and Figure 3.11 describe the timing of the calibration states.

Table 3.3.: Front End States

State Name	Duration (sec)
Phase Calibration	1
Antenna Through	9
Noise Calibration	2
Antenna Swap	8

The four calibration states are as follows: Phase Calibration, Antenna Through, Noise Calibration, and Antenna Swap. The calibration states repeated every 20 seconds. The earth antenna channel was swapped between alternate polarizations every 15 minutes. In 2017, the phase calibration state was not activated for the 2017 experiment. Figure 3.12 shows the 2017 calibration state timing.

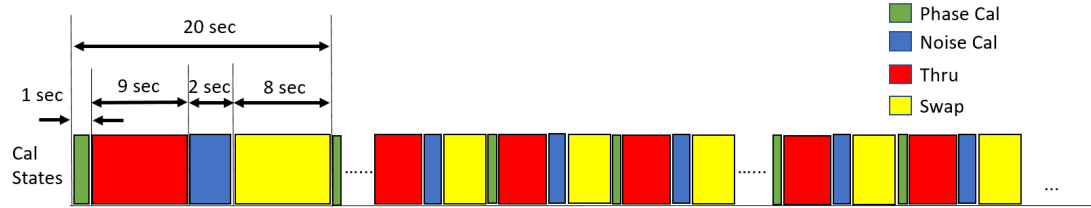


Fig. 3.11.: 2018 Front End Timing Diagram

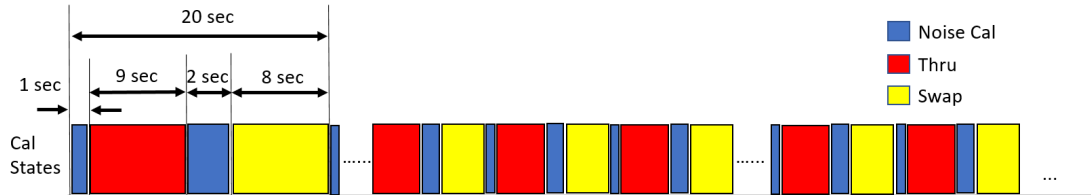


Fig. 3.12.: 2017 Front End Timing Diagram

3.2.4 Temperature Sensors

For instrument calibration purposes, 100Ω Resistance Temperature Detectors (RTD) sensors were placed on the 50Ω terminators. Sensors were also placed on the amplifiers for monitoring their temperature. Sensors were installed on the three amplifier models in the front end. The RTD sensors were connected to an ADAM-4015 data logger which digitized the analog signal and communicated with the Raspberry Pi host computer via RS-485.

3.3 Link Budget

A link budget was performed to estimate the signal to noise ratio for S and P band. The brightness temperature is different for the sky and earth antennas. The link budget analysis is provided in Table 3.5.

Free space loss:

$$L_0 = 20 \log_{10} \left(\frac{4\pi R}{\lambda} \right) [dB] \quad (3.1)$$

- *EIRP*: “Effective Isotropic Radiated Power,” a function of the transmitter power, amplification and antenna gain.
- L_A : Atmospheric attenuation. Constant for a given wave length.
- G_R : Receiver Gain. Includes antenna gain and amplifier gain.
- L_R : Receiver Losses. Includes cable loss and impedance mismatch of microwave comments.

The Received Power equation: a summation of transmitted power, signal loss, and signal gain.

$$P_r = EIRP - L_0 - L_A + G_r - L_r \text{ [dBW]} \quad (3.2)$$

Microwave systems have wide band noise from multiple sources, include thermal background noise. T_R is the equivalent noise temperature of the receiver system.

Antenna brightness temperature is modeled as:

$$T_{ant} = \frac{\int_0^{2\pi} \int_0^\pi T_B(\theta, \phi) D(\theta, \phi) \sin\theta d\theta d\phi}{\int_0^{2\pi} \int_0^\pi D(\theta, \phi) \sin\theta d\theta d\phi} \quad (3.3)$$

where $D(\theta, \phi)$ is the antenna gain pattern, T_B is the background temperature. Following convention, the ground brightness temperature was chosen to be 290 K, the horizon was chosen to be 75K and the sky was chosen to be 5K [19]. Table 3.4 shows calculated antenna noise temperatures for the antennas in the experiment. The simulated gain pattern was used for P-Band, the published values for S-Band antennas published gain pattern values.

Receiver Noise Equation:

$$N_R = 10\log_{10}((T_R + T_{ant})Bk) \quad (3.4)$$

where: B is bandwidth of the front end, k is Boltzmann’s constant.

Table 3.4.: Noise Temperatures for Antennas

Antenna	Noise Temperature
XM Sky	5 K
XM Earth	290 K
P-Band Sky	7.718 K
P-Band Earth	294.28 K
P-Band Horizontal	151.6 K

Table 3.5.: Link Budget for Purdue SoOp Tower Experiment

	P Band	S Band 2017	S Band 2018	Units
Signal Name	MUOS	XM Radio	XM Radio	
Bandwidth	5	1.84	1.84	MHz
EIRP	47	68	68	dBW
Range	37,682	37,535	37,535	km
Free Space Loss	175.33	191.34	191.34	dB
Atmospheric loss	0.5	0.5	0.5	dB - Arbitrary
Polarization Loss	3	0	0	dB
Antenna Gain	6.8	3	3	dBi
Power at Frontend	-124.0	-125.83	-125.83	dBW
Noise Temperature System	316.51	329.38	62.67	K
CN0	9.72	20.14	27.731	dB

3.4 Equipment Shed

Two temperature controlled equipment cabinets are installed on the bed of the tower trailer. The phase calibration system, digital recording equipment, DC voltage supplies and support equipment were installed in a single cabinet. The cabinet's were

powered with a 30 Amp, 120V electrical service as well as an optical fiber network for connection to Purdue's computer network. An uninterruptible power supply was installed to compensate for short power interruptions.

3.4.1 Phase Calibration Unit

From a previous experiment conducted by the Radio Navigation Lab, it was observed that the Ettus B210 Digital recording units would induce a random phase offset between the 2 input channels each time a recording session started. A phase calibration unit was designed such that a phase shift due to the USRP could be detected and calibrated out. A Mini-Circuits MTS-18-12+ reflective switch was used with a Mini-Circuits Z99SC-62-S+ power splitter for P-Band and a Mini-Circuits ZAPD-2-272-S+ for S-Band.

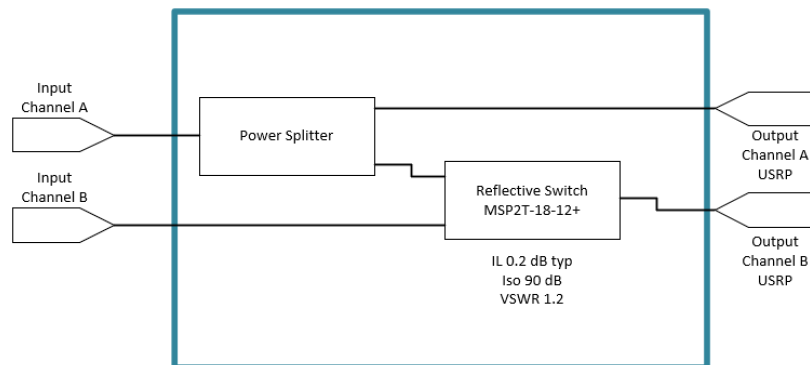


Fig. 3.13.: Phase Calibration Unit

3.4.2 Digital Receiver

For both signals, a Ettus Universal Software Defined Radio B210 unit were used to digitize the RF signals. The B210 performs the necessary processes for direct-conversion of RF to digital in the range of 70 MHz to 6 GHz up to 56Mhz of band-

width. The B210 has 2 recording channels, enabling a single unit to record both the direct and reflected signal. Each B210 was connected to a Intel “Next Unit of Computing” (NUC) desktop computer via USB 3.0. The NUC’s used a Linux OS (Ubuntu 16.04 LTS in 2017/18.04 LTS in 2018) for their operating system. The computers ran custom recording software for the USRP. 8TB external hard drives were used to temporarily store the data and for physical transportation between the experiment site and Purdue university for long term storage and processing.

3.4.3 Relay Controller

A Raspberry Pi was used to control a simple relay circuit controlling the front end calibration states as shown in Figure 3.11. The Raspberry Pi also used a RS-485 to TTL logic converter for communicating with the ADAM datalogger for the temperature sensors.

3.5 Data Management

The experiment generated approximately 11.13 TB a week of raw sample data. Table 3.6 summarizes the data storage requirements. The recording computers copied the data off onto external USB hard drives. The hard drives were retrieved weekly and copied onto Purdue’s tape based data archive system. The hard drives were then stored as a second, redundant backup.

Table 3.6.: Recording Data Rate

Signal	Sample Rate	Bytes per Sample	Minutes Per Hour	TB per Week
P-Band	30 MHz	2	6	3.87
S-Band	4 MHz	4	6	7.26

4. FIELD EXPERIMENT



Fig. 4.1.: 2018 Field Experiment Tower Setup

Two field experiments were conducted during the summers of 2017 and 2018 at Purdue's Agronomy Center for Research and Education (ACRE) in field #23, West Lafayette, IN. This location is conveniently located close to Purdue University's West Lafayette campus and had access to electrical power and internet access. The field

experiments had minor sensor location variations between years 2017 and 2018 as explained below. The soil in field #23 was loam type. The cornfield had drainage tiles installed 1 m below the surface to assist in water drainage. The tiles ran east to west and spaced 20 m apart north to south.

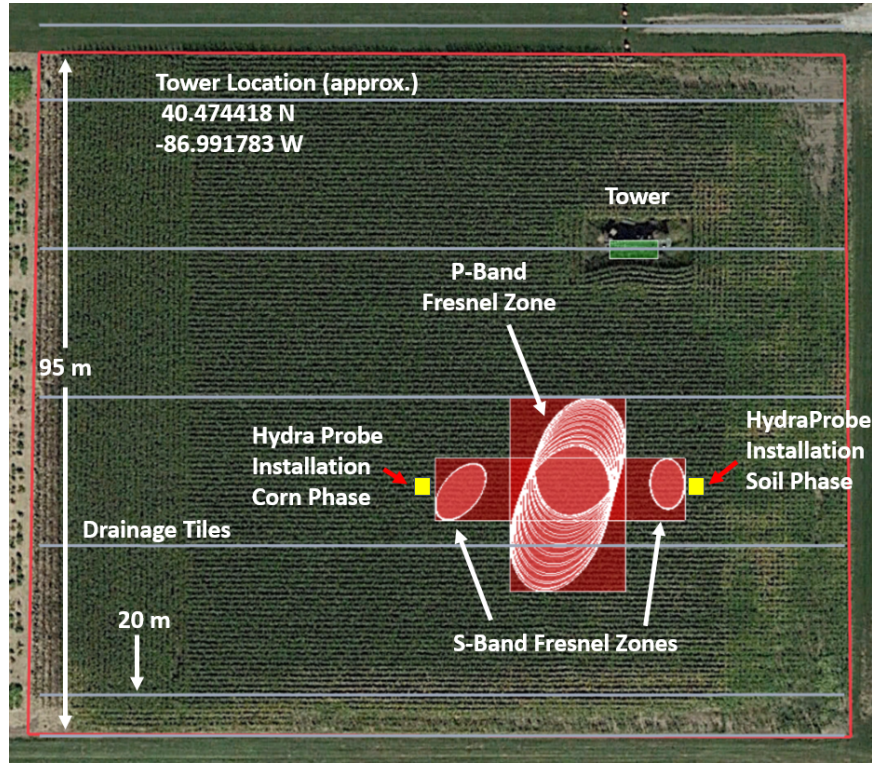


Fig. 4.2.: 2017 Experiment Map: In Situ Sensor Locations and Estimated Fresnel Zones

4.1 2017 Sensor Placement

Figure 4.2 depicts the tower, specular point locations and HydraProbes installation for the 2017 experiment. The satellite image is from September of 2017. The tower location was designed to place the specular points at the midpoint between the drainage tiles. The long edge of trailer was oriented perpendicular to azimuth. The green box on the image represents the calculated location of the tower, the satellite

image confirmed we placed the trailer in the correct location in the field. There were only a single set of four HydraProbes installed for the 2017 growth season, installed at the midpoint between the two drainage tiles. They were initially installed to the right of the specular points for the bare soil observation, but were moved to the left side of the specular point after the corn was planted. The probes were moved to be representative of the corn growth in the specular point, away from the corn end-rows.

4.1.1 Antenna Orientation

Both P-Band antennas were placed in the vertical polarization as shown in Figures 4.3 and 4.4. The sky antenna was oriented to +41 elevation to place the gain pattern null towards the specular point. The earth antenna was oriented to -41 elevation to place the gain pattern null toward the transmitter source. These orientations were chosen to maximize the signal isolation between the sky and earth antennas. The P-Band antennas were oriented towards 200° azimuth to face the transmitter and specular point.

The XM antennas were placed on horizontal 2x4 ft aluminum plates facing the sky and the earth. The gain pattern of the XM antennas allowed for near perfect isolation between the direct and reflected signals. Figure 4.5 and 4.6 show the orientation of the antennas and front end for the 2017 field campaign.

4.2 2018 Sensor Placement

In 2018 the tower was placed as shown Figure 4.7, approximately 10 feet further west than 2017. The tower was moved further west into the field to move the specular points away from the corn end rows. Two sets of four HydraProbes were installed, one set over the drainage tile and the other midpoint between two drainage tiles. The second set of hydra probes were added to measure the soil moisture profile between the drainage tiles. The trailer was oriented perpendicular to the 200° azimuth to simplify the antenna pointing processes.

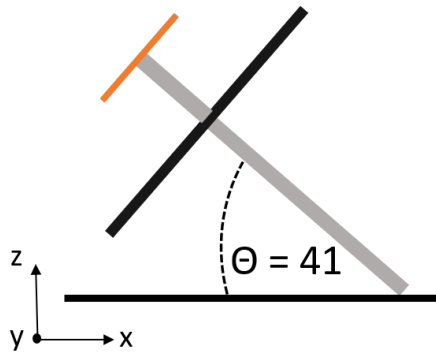


Fig. 4.3.: Sky Oriented Vertical P-Band Antenna

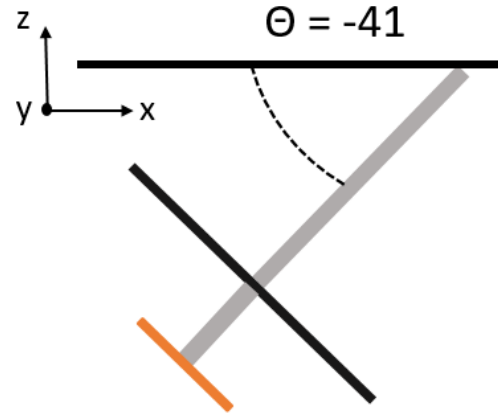


Fig. 4.4.: 2017 Earth Vertical P-Band Antenna

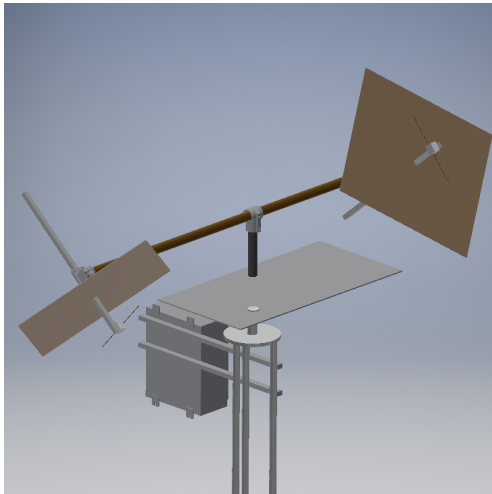


Fig. 4.5.: 2017 Tower Top View

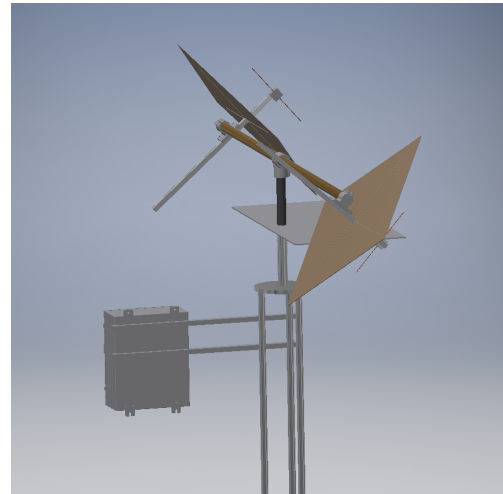


Fig. 4.6.: 2017 Tower Top View

4.2.1 Antenna Orientation

The antenna placement on the tower was modified from 2017, placing the S-Band antennas on two smaller aluminum plates as shown in Figures 4.8, 4.9. Three P-Band antennas were used in 2018. The sky antenna had the same orientation as in 2017,

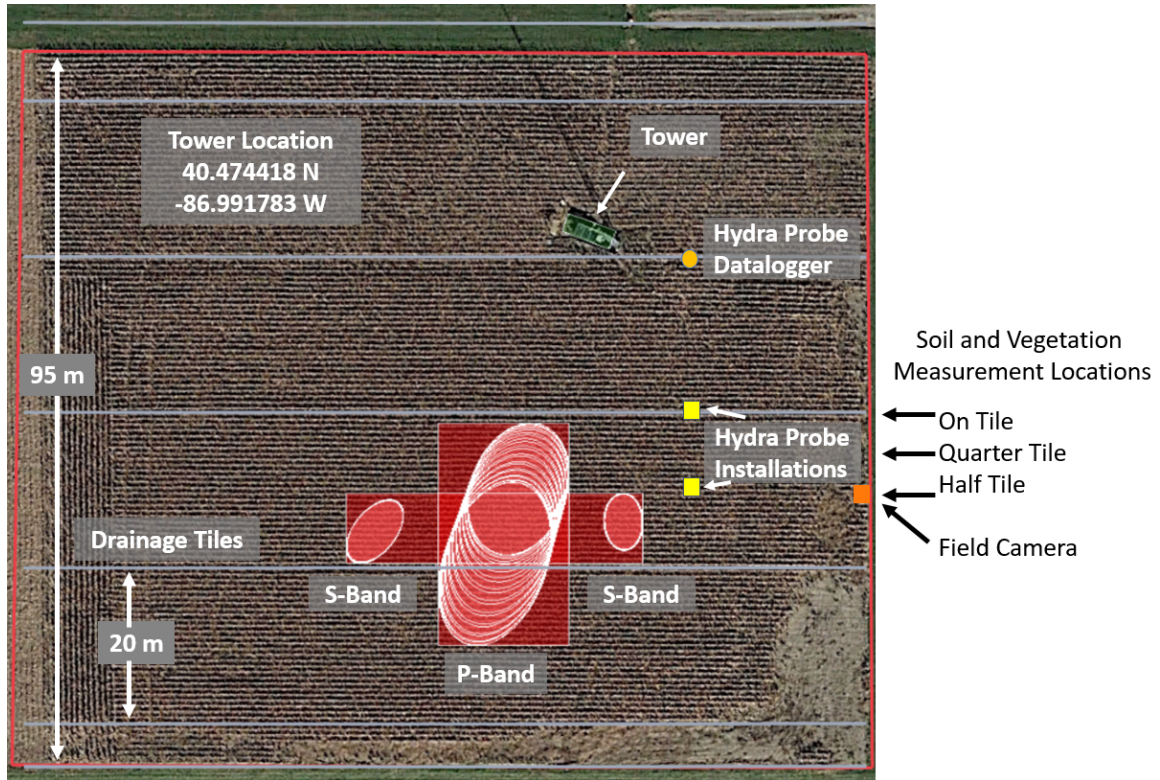


Fig. 4.7.: 2018 Experiment Map: In Situ Sensor Locations and Estimated Fresnel Zones

shown in Figure 4.3. Two earth antennas, horizontally and vertically polarized were oriented towards the horizon as shown in Figures 4.10 and 4.11.

4.3 In Situ Truth Measurements

The sampling protocol was modeled after the Soil Moisture Experiment 2005 (SMEX05) as discussed in [20]. The corn growth was monitored with distinctive measurements. A soil moisture measurement protocol was designed to collect calibration data for the in situ HydraProbes. A blank example of the soil and vegetation data collection sheet used in the 2018 field experiment is provided in Appendix C.



Fig. 4.8.: 2018 Sky S-Band Antenna



Fig. 4.9.: 2018 Earth S-Band Antennas

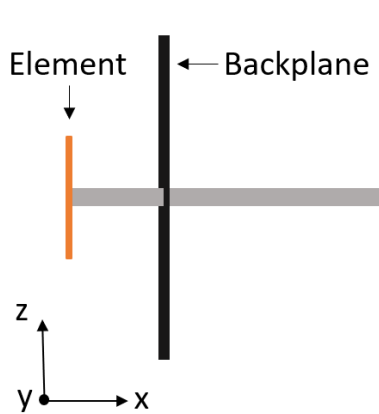


Fig. 4.10.: 2018 Earth Vertical P-Band Antenna Orientation

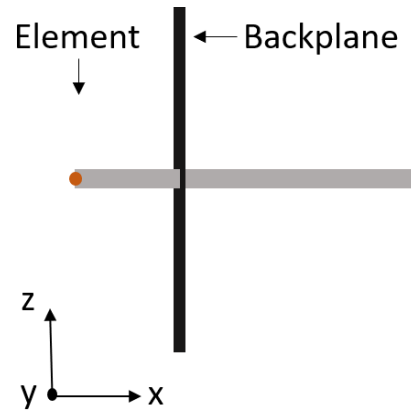


Fig. 4.11.: 2018 Earth Horizontal P-Band Antenna Orientation

4.3.1 In Situ Soil Moisture Sensors

HydraProbes measure soil dielectric permittivity, salinity and temperature via transmitting a 50 Mhz radio frequency signal [21]. The HydraProbes were installed

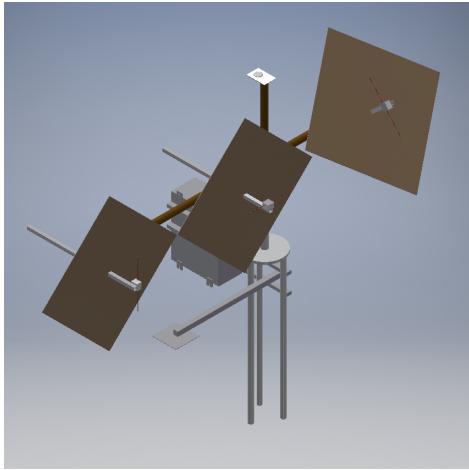


Fig. 4.12.: 2018 Tower Top View

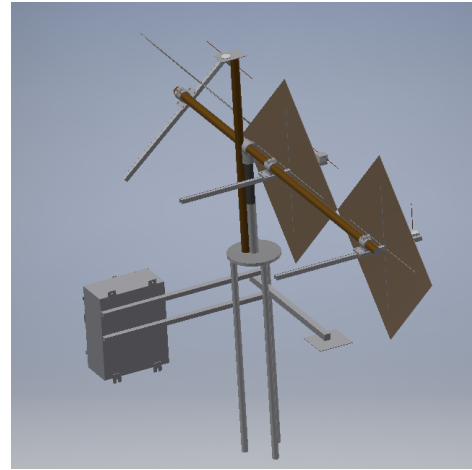


Fig. 4.13.: 2018 Tower Top View

before the corn was planted, removed and reinstalled for the planting of corn and then removed and reinstalled for the corn harvesting. Soil samples were taken at weekly intervals to provide empirical data for calibration of the hydra probes.

Both measurement locations had a probe installed at 5, 10, 20 and 40 cm below the surface of the soil. A Campbell Scientific CR300 data logger was used to interface with the HydraProbes. Measurements were taken every 15 minutes of the 4 hydra probe analog voltages and the complex dielectric measurement. The HydraProbe sensors were installed directly over the northern drainage tile and 1/2 way between the northern and southern drainage tile (with respect to the specular point) as shown in Figure 4.2. A pit was dug slightly deeper than 40 cm, the northern side of the wall was made to be flat. The HydraProbes inserted into the soil face at their appropriate depths. Each probe was placed a horizontal distance apart, such that the vertical flow of the water was not disrupted. Figure 4.14 shows the installation of a set of HydraProbes.

In 2017 a single set of HydraProbes were installed at the midpoint between the drainage tiles. After visually observing that after a rain event the field would drain quicker over the drainage tiles than the rest of the field, it was decided to add another set of HydraProbes for 2018. The two sets of HydraProbes were installed over the

drainage tile and at the midpoint between the two drainage tiles at the same depths as shown in Figure 4.7.



Fig. 4.14.: HydraProbe Installation - 2018 Field Experiment

4.3.2 Gravimetric Soil Sampling

Gravimetric soil samples were collected on a weekly interval. A soil probe was used to extract soil at 5cm, 10cm, 20cm and 40cm. The soil samples were collected and placed in sample tins. The samples were transported from the experiment site to the National Soil and Erosion lab on Purdue's campus where they were weighed and dried.

4.3.3 Theta Probe

A handheld theta probe was used to measure surface soil moisture at each sampling location of the surface soil moisture. The probes of the instrument are about 4 inches long. The probes were inserted vertically into the soil. Three measurements were made at each sampling point: in the corn row, 1/4 row and 1/2 row as shown in Figure 4.15

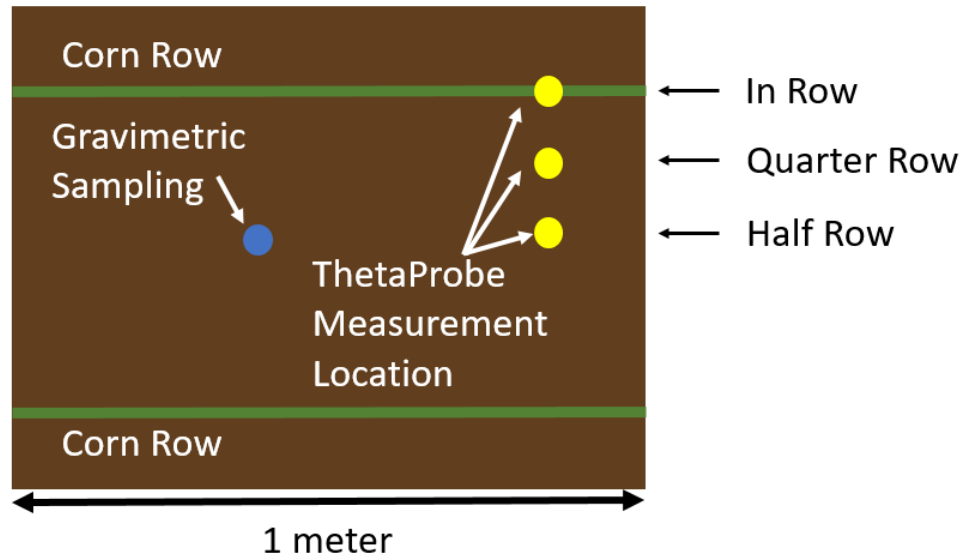


Fig. 4.15.: In Row Sampling Locations

4.3.4 Crop Measurements

Crop growth measurements were conducted weekly with the gravimetric soil sampling. Three plants were picked within one meter that represented the average for the sampling area. The number of corn plants per m^2 , row spacing, plant height, stalk diameter, number of leaves, number of cobs, leaf height and length from the bottom, middle and top leaf were measured. The measurements were made in the field, then the plants were removed and taken back to Purdue's Indiana Corn and Soybean Innovation Center where the plant was separated into the stalk, leaves and cobs. For each sampling site, the 3 plants were placed in brown paper bags, weighed, dried in Wisconsin ovens then weighed again to determine water weight.

4.3.5 Inferred Vegetation Measurements

In 2018, the addition of Inferred was added to the crop measurements. A Rapid-Scan CS-45 hand held inferred NVDI and NDRE sensor was measured until 8/11/2018. The unit recorded 670 nm, 730 nm and 780 nm wavelength and had a differential GPS

unit to tag the location data. The RapidScan is a handheld unit designed to take NVDI measurements of grass, when the corn grew past 4 feet we were not able to take measurements in the field with the RapidScan. It was planned to mount the unit on a pole, but experiment priorities took precedent over designing a mounting pole.

5. IN SITU OBSERVATIONS

5.1 2017 Observations

5.1.1 Soil Moisture

The calibrated 2017 Hydra Probe data is shown in Figure 5.1.

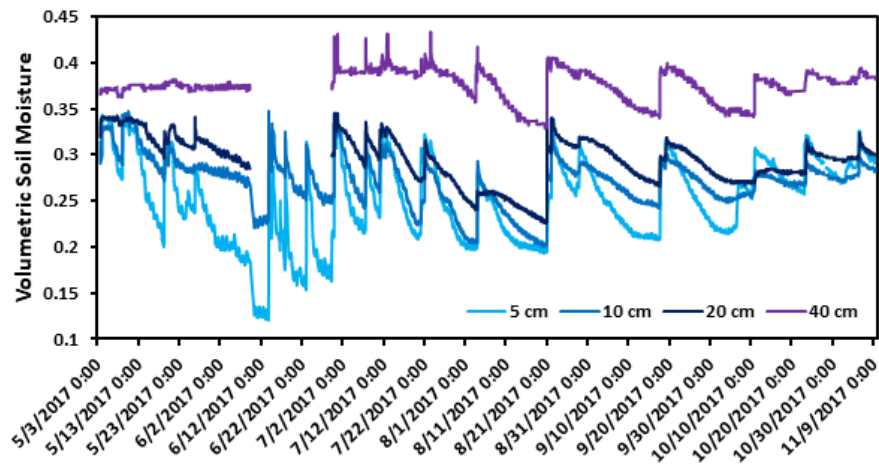


Fig. 5.1.: 2017 HydraProbe Soil Moisture

5.1.2 Vegetation

In 2017 the row spacing was 76.5 cm and the plant spacing was 15.24 cm. The corn distribution was assumed to be uniform over the entire field giving an average of 8.61 *plants/m*². The 2017 vegetation water content of corn is shown in Figure 5.2.

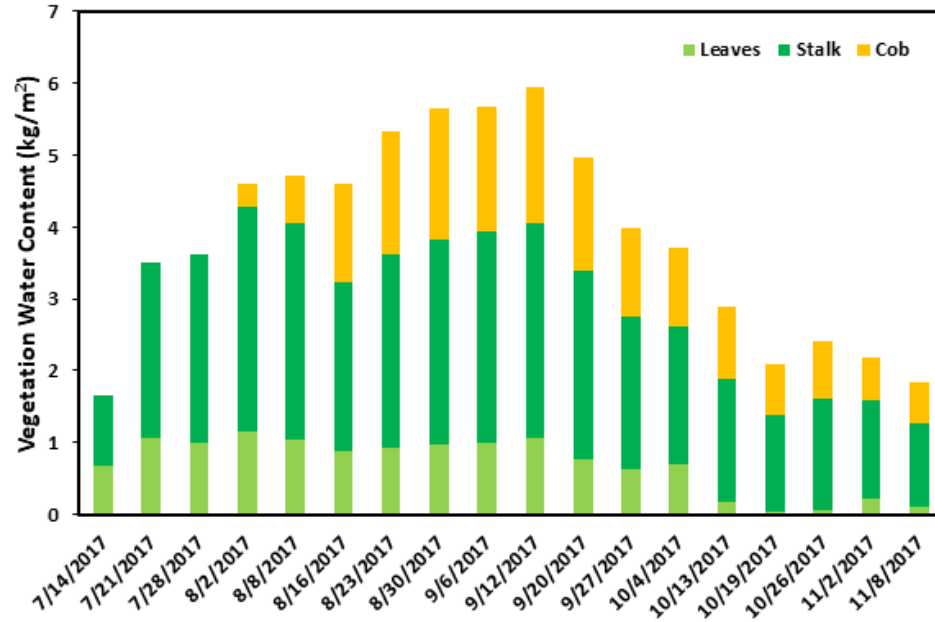


Fig. 5.2.: 2017 Vegetation Water Content

5.2 2018 Observations

The uncalibrated soil dielectric measurements from the HydraProbes are shown in Figures 5.3, 5.4. The right hand Y axis is precipitation data from the Purdue ACRE weather station [22].

5.2.1 Gravimetric Soil Moisture

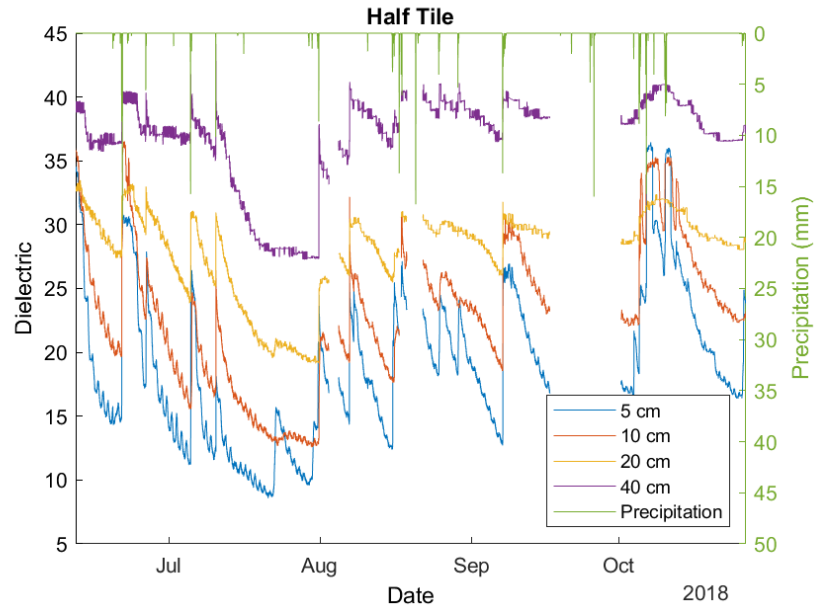


Fig. 5.3.: Precipitation and HydraProbe Dielectric Readings - Half Tile Location

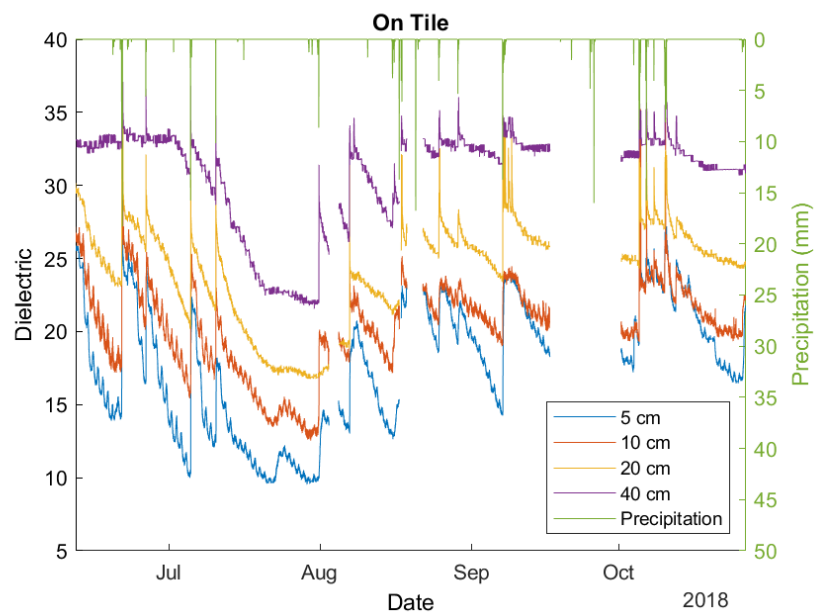


Fig. 5.4.: Precipitation and HydraProbe Dielectric Readings - On Tile Location

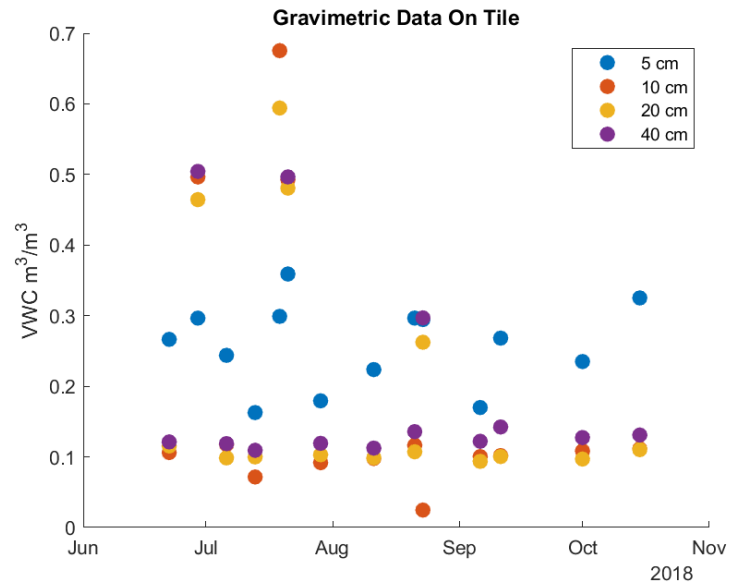


Fig. 5.5.: On Tile Soil Moisture Measurements

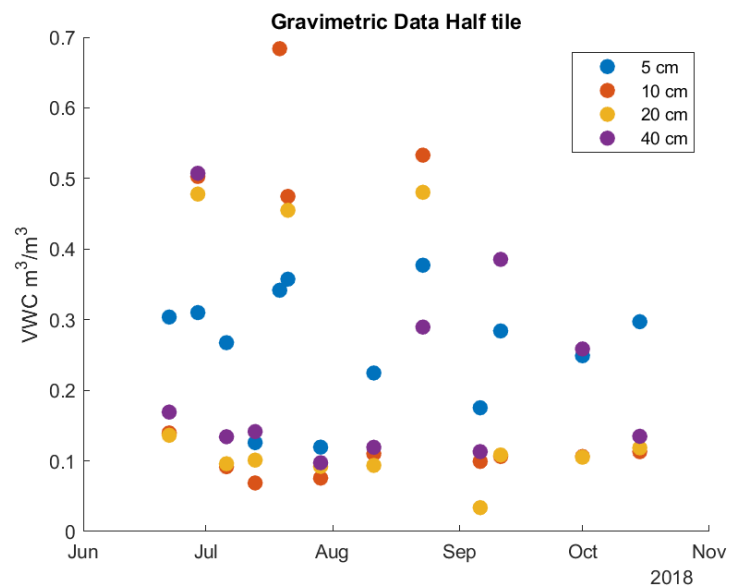


Fig. 5.6.: Quarter Tile Soil Moisture Measurements

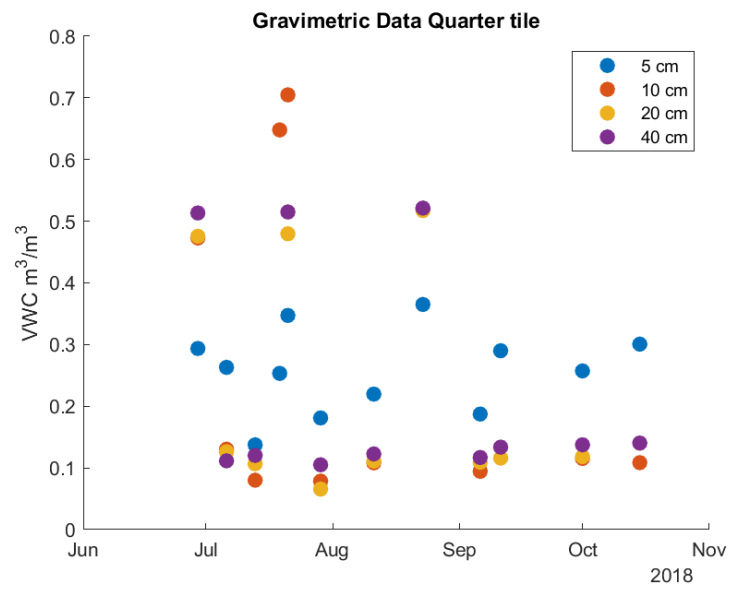


Fig. 5.7.: Half Tile Soil Moisture Measurements

The corn row spacing for 2018 was 73 cm. Each data collection the number of corn plants per m^2 was counted. The average corn distributions for the three measurement locations are shown in Table 5.1.

Table 5.1.: Plants per m^2 - 2018

Measurement Location	$plants/m^2$
On Tile	19.82
Quarter Tile	19.82
Half Tile	19.36

Vegetation Water Content of Corn for 2018 is shown in Figures 5.8 to 5.10.

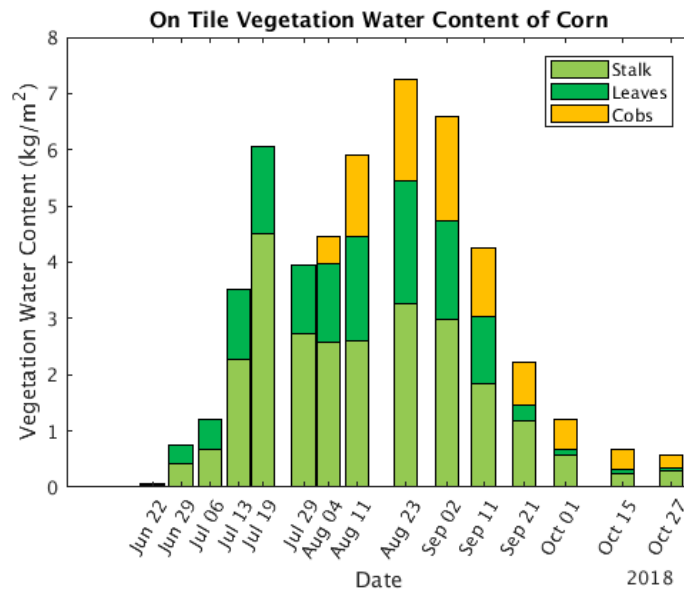


Fig. 5.8.: 2018 Vegetation Water Content - Drainage Tile

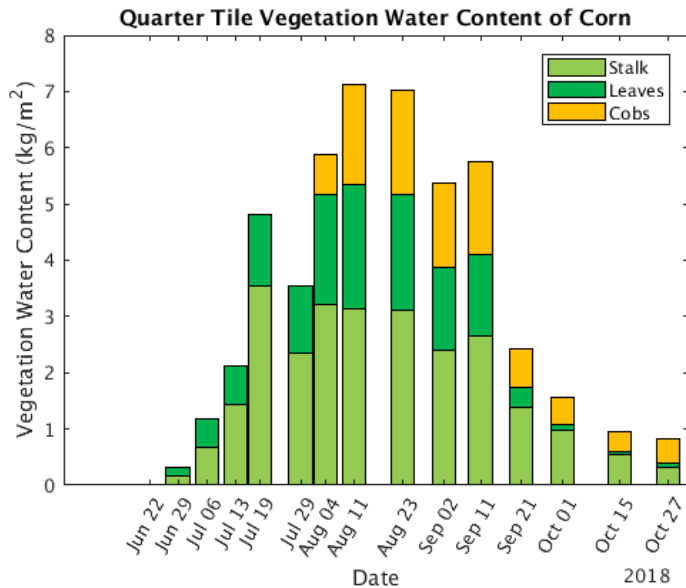


Fig. 5.9.: 2018 Vegetation Water Content - Quarter Tile

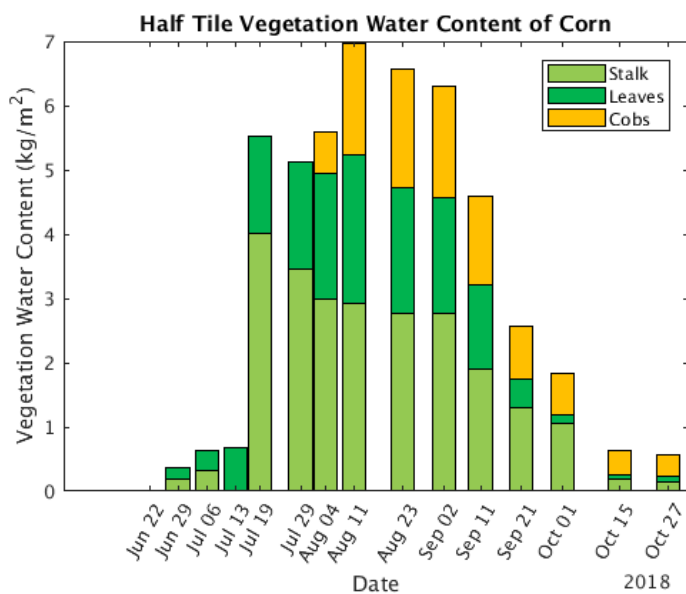


Fig. 5.10.: 2018 Vegetation Water Content - Half Tile

6. EXPERIMENT SUMMARY

6.1 Instrument Changes Summary

Item	2017	2018
S-Band RHCP earth antenna	✗	✓
Horizontal P-Band earth antenna	✗	✓
Noise recording	✗	✓

Table 6.1.: Key instrument changes by year

6.2 Timeline of Major Events - 2017 Experiment

2017 Field Campaign Timeline		
Date	Event	Notes
5/23	Campaign Start	
6/09	Pause for corn planting	Tower lowered, front end removed for hardware additions
		P-Band horizontal polarization reflected antenna added to tower and front end S-Band RG-8 cables had incorrect connectors, S-Band data was not recorded
7/08	Microwave recording resumed	Code bug in calibration states, horizontal P-Band state not activated
7/11	Wind storm - tower damaged	Microwave recording stopped, tower lowered
		P-Band antenna ground plane mesh changed to chicken wire
10/10	Recording resumed	Tower was only tilted (10 m high) due to damaged frame
11/04	Campaign end	

Table 6.2.: 2017 Campaign Timeline

2018 Field Campaign Timeline		
Date	Event	Notes
5/29	Campaign start	
5/30	P-Band amplifier failed	ZX60-P103LN+ failed, unknown reason
6/23	Began noise recording	
Removed ZX60-P103LN+ only from P-Band amplifier chain, P-Band front end returned to 2017 configuration		
6/27	P-Band front end repaired	
7/09	Temperature sensors stopped recording	Unknown reason
8/11	Last NVDI Measurement	
9/01	Temperature sensors recording resumed	Raspberry Pi restart
10/21	Severe winds, tower damaged	
10/27	Campaign ends	

Table 6.3.: 2018 Campaign Timeline

6.3 Timeline of Major Events - 2018 Experiment

The Campbell data logger had several “no-data” collection periods due to a dead battery. A list of these events is shown in Table 6.4

Data Logger Dead Battery Events	
Begin	End
6/5 13:00	6/7 11:30
8/02 18:15	8/4 18:00
8/17 4:00	8/21 23:15
9/16 22:0	10/01 11:30

Table 6.4.: Data Logger Dead Battery Events

6.4 Validation of Microwave Data

The microwave data was verified from the ambiguity functions of the data. The path distance between the direct and reflected signal is calculated:

$$2(32m)\sin(41^\circ) = 41.98m \approx 42m \quad (6.1)$$

The Self Ambiguity Function (SAF) is the auto correlation estimate as given in Equation 2.34. The cross correlation is for the through calibration state as given in Equation 2.36. In the following plots, the integration time $T_I = 10$ ms. All of the plots are a single 10 ms results (no incoherent averaging).

6.4.1 P-Band

The ambiguity functions show that the instrument recorded the MUOS signal in the direct channel. The reflected channel recorded both the direct signal and a time delayed version of the direct signal (the reflected signal). The cross correlations between the direct and reflected signals has two peaks, with the separation between the peaks consistent with the path distance as found in Equation 6.1.

- In Figure 6.1 for both the direct and reflected PSDs, Radio Frequency Interference (RFI) is present between -15 to -10 MHz and at 10 MHz. The earth antenna is horizontally polarized.
- In Figure 6.2. The cross correlation plot shows two peaks, this is expected as the horizontal earth antenna captures both the direct and reflected signals. The peaks of the plots are separated by approximately 40 m. The noise SAF is a sinc function as expected.
- In Figure 6.3 for both the direct and reflected PSDs, Radio Frequency Interference (RFI) is present between -15 to -10 MHz and at 10 MHz. The earth antenna is Vertically polarized.

- In Figure 6.4. The cross correlation plot shows two peaks, this is expected as the horizontal earth antenna captures both the direct and reflected signals. The peaks of the plots are separated by approximately 40 m. The noise SAF is a sinc function as expected.

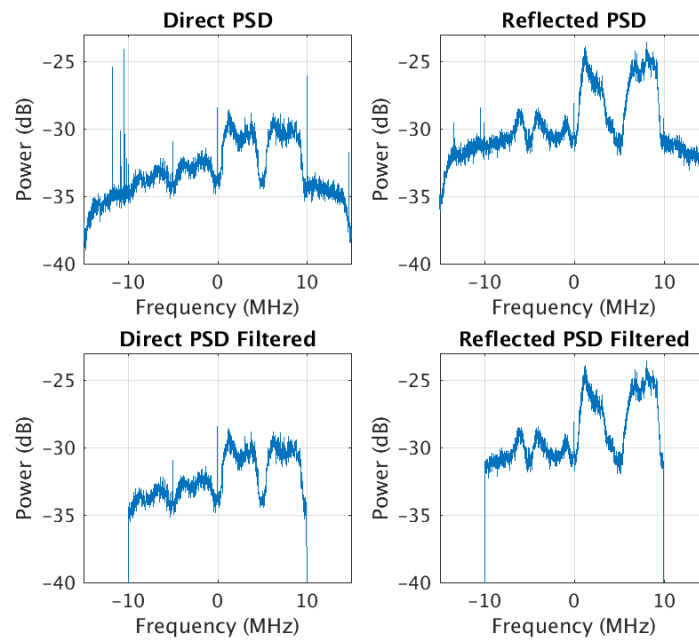


Fig. 6.1.: MUOS Spectrum, Centered at 370 MHz - 6/29/18 14:00

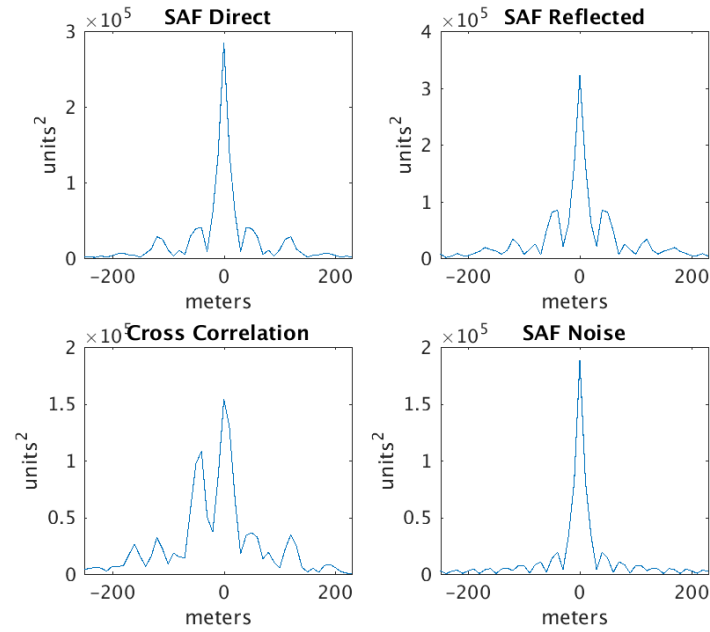


Fig. 6.2.: MUOS Ambiguity Functions - 6/29/18 14:00

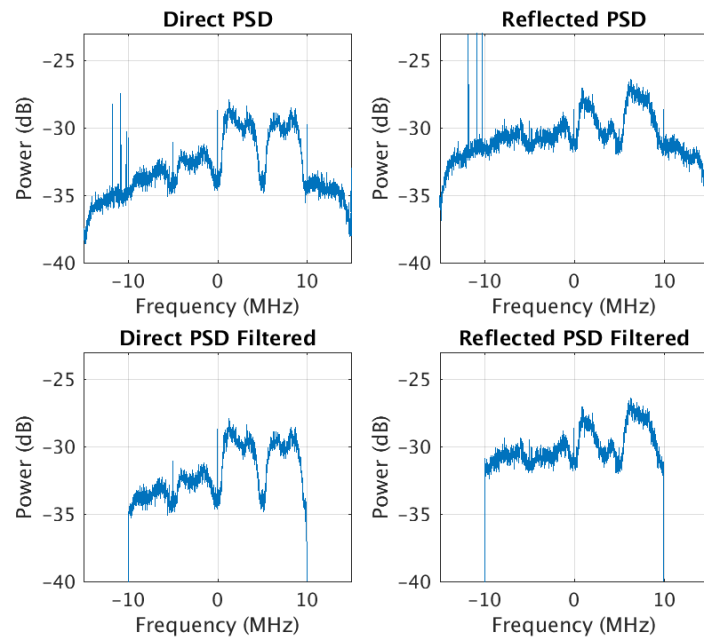


Fig. 6.3.: MUOS Spectrum, Centered at 370 MHz - 6/29/18 14:15

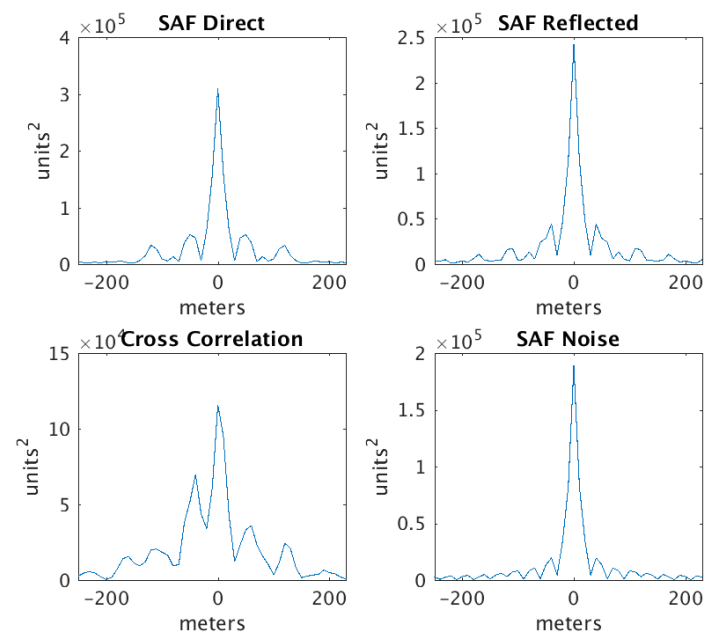


Fig. 6.4.: MUOS Ambiguity Functions - 6/29/18 14:15

6.4.2 S-Band

The ambiguity functions show that the instrument recorded the XM signal in the direct channel and the reflected channel recorded a time delayed version of the direct signal. The cross correlations between the direct and reflected signals is a single peak, with the peak locations consistent with the path delay as found in Equation 6.1.

- In Figure 6.5, there is RFI present at approximately 3 MHz.
- In Figure 6.6. The cross correlation plots shows a single peak at approximately 37.5m. The noise SAF is a sinc function as expected.
- In Figure 6.7, there is RFI present at approximately 3 MHz.
- In Figure 6.8. The cross correlation plots shows a single peak at approximately 37.5m. The noise SAF is a sinc function as expected.

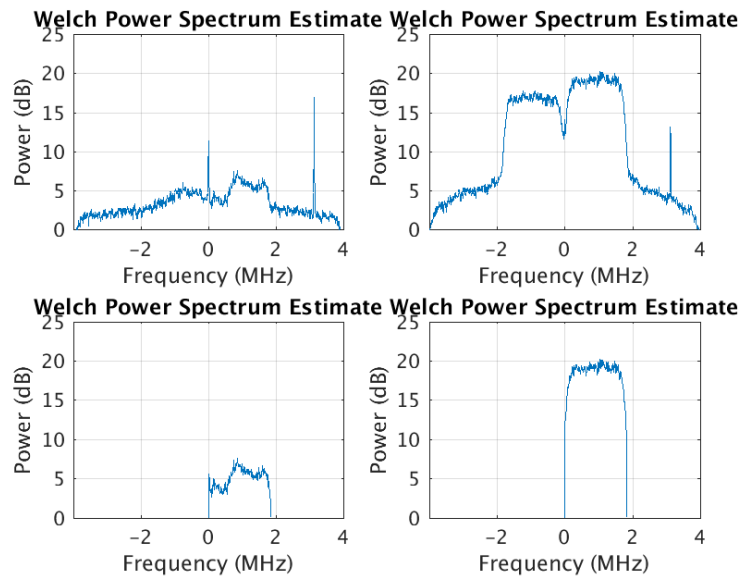


Fig. 6.5.: XM Spectrum, Centered at 2.344 GHz - 8/02/18 15:00

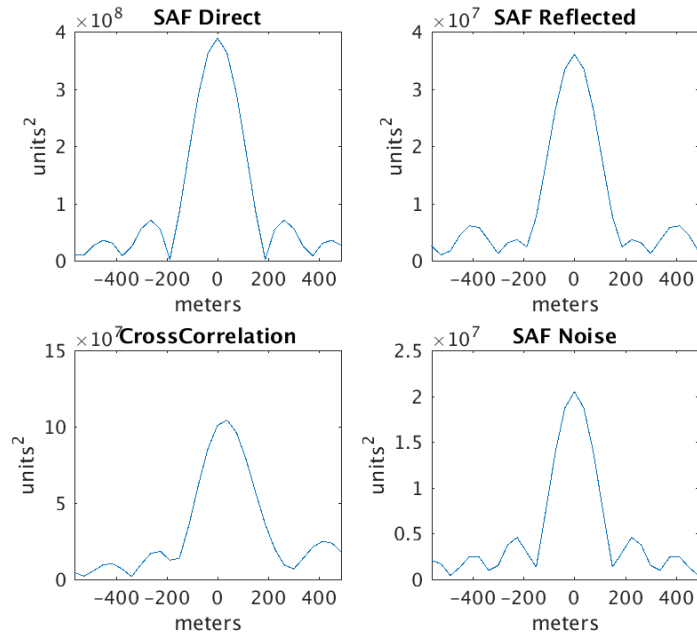


Fig. 6.6.: XM Ambiguity Functions - 8/02/18 15:00

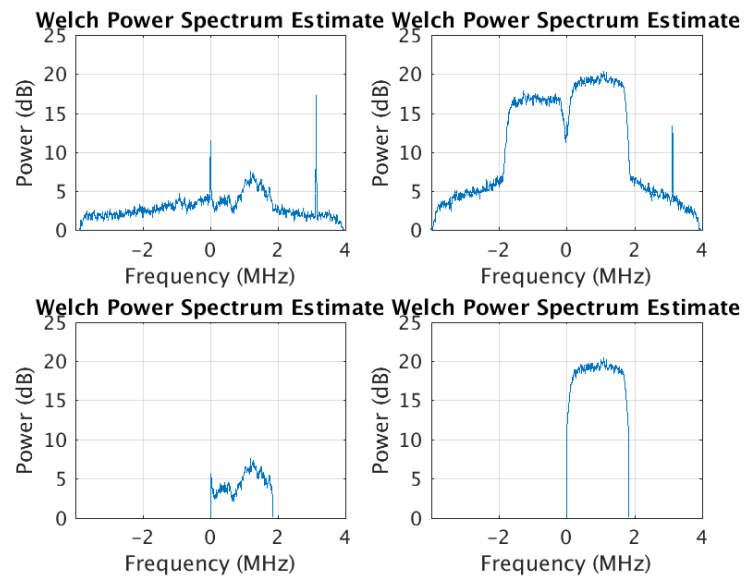


Fig. 6.7.: XM Spectrum, Centered at 2.344 GHz - 8/02/18 15:15

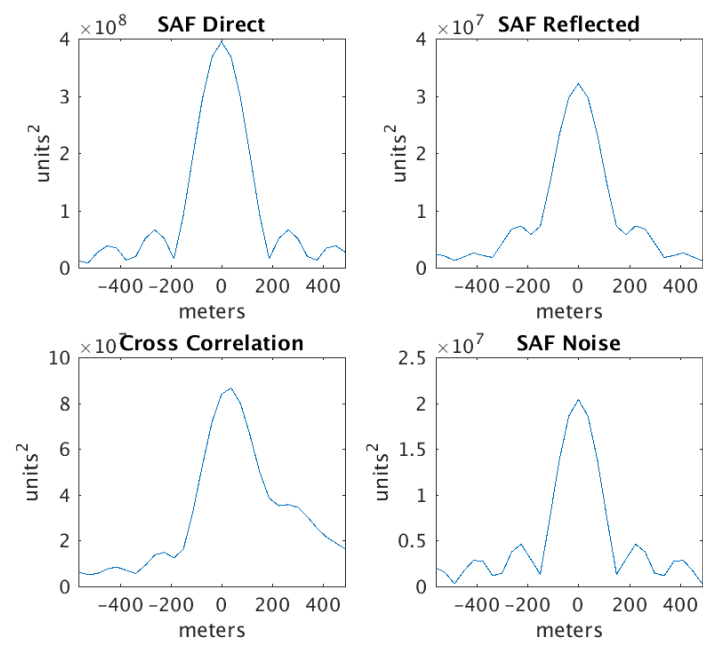


Fig. 6.8.: XM Ambiguity Functions - 8/02/18 15:15

6.5 Recommended Instrument Improvements

After running two field campaigns, the following improvements are recommended for future field experiments.

6.5.1 Microwave Hardware Improvements

A lower noise figure P-Band amplifier system should be designed. This was attempted in 2018, but the first set of low noise amplifiers failed due to an unknown cause.

Narrower P-Band filters should be used to mitigate receiving out of band transmissions. The 2018 P-Band system originally used a Mini-Circuits ZX60-P103LN+ as the first amplifier in the P-Band front end. A hypothesis of the failure of those amps is they were over saturated from out of band RF signals.

DC blocks should be installed before the amplifiers and the P-Band antennas. In the event that a short would happen from the P-Band dipole antennas (either water leaking into the box or a short from the elements touching), this would block the short to the amplifiers.

Commercial antennas that operate in the P-Band range should be purchased to replace the dipole antennas. Log-periodic antennas are easily obtainable that operate in the P-Band range. Their gain patterns are well understood and they have good impedance matching.

Lower loss cables between the antennas and the front end. This would reduce the instrument noise figure.

The front end should be painted white to reflect heat which would reduce the noise floor of the instrument. The front end should also be wrapped in the bubble wrap/foil reflectors that are used in cars to further reduce the heat from the sun.

Temperature controlled front end via a thermometric module. This would keep the system gain stable and lower the thermal noise from the amplifiers.

To allow for an absolute gain calibration of the microwave front end, a diode noise source should be added to the calibration states.

6.5.2 In-situ instrument Improvements

A third set of HydraProbes should be installed over the quarter tile location to obtain a more complete soil moisture profile.

A simple weather station should be installed near the tower. The Purdue ACRE weather station's data had time periods in 2018 where there was no data.

A temperature sensor should be installed for measuring the ambient temperature around the trailer.

The Campbell data logger for the HydraProbes should be connected to DC power direct from the trailer. There were several extended periods of time the data logger was not recording due to dead batteries. If a third set of hydra probes is installed for the next field camping, the batteries for the data logger would not last an entire week.

A high precision GPS unit should be used to make the locations of the experiment instruments. For example the hydra prob installations, field camera, weekly in-situ corn and soil measurements, etc.

Install a second field camera partially up the tower, but far enough away from the antenna to avoid introducing RFI, facing the specular point. This would be helpful to see the corn growth.

A handheld RapidScanner was used to measure the NDVI of the corn in 2018, but measurements stopped being taken once the corn grew taller than about 4 feet. A mounting pole could be used to elevate the crop scanner above the corn to take measurements throughout the entire growth cycle.

A CropScan NVDI instrument should be purchased to replace the RapidScanner to capture a larger light spectrum.

6.5.3 Software Improvements

The USRP PC's and Raspberry Pi should "call home" on a daily basis. Either an automated email or SCP transfer detailing hard drive free space, recording software status, etc. Many of the gaps in the data recording could have been avoided if the PC's status was checked daily.

Setup a script to daily run the "quickLook" script on a raw data file and email the result to be reviewed. This would be a check on the microwave hardware operation.

6.6 Conclusions

This thesis designed and assembled a remote sensing instrument that used Signals of Opportunity. The instrument used two signals in P-Band and S-Band for measuring soil moisture and above ground biomass. It was mounted on a tower and used during two data campaigns in 2017 and 2018. The data campaigns created a data set in a controlled experiment environment with in situ observations of soil moisture and above ground biomass.

Learning from the challenges experienced during the 2017 field campaign, changes were made to the instrument for the 2018 field campaign. Improvements to the microwave system included a lower noise front end and improvements to the antenna mounting on the tower. The mechanical aspects of the tower were also improved in 2018, reducing the sizes of the S-Band antenna mounting plates and the addition of guy-wires to improve the tower structural integrity during wind events. The in situ observations were also expanded to accommodate a non-uniform experiment location.

The data from the two field campaigns will be analyzed and used to create soil moisture and above ground biomass retrieval models. Future field campaigns are planned for the instrument incorporating the improvements discussed in this section. The data sets from 2017 and 2018 will be used to improve the instrument and in support of Snoopi, a cubesat based spaceborne version of this instrument.

REFERENCES

REFERENCES

- [1] “Essential Climate Variables.” [Online]. Available: <https://public.wmo.int/en/programmes/global-climate-observing-system/essential-climate-variables>
- [2] “GCOS Land ECV - Above Ground Biomass.” [Online]. Available: <https://www.ncdc.noaa.gov/gosic/gcos-essential-climate-variable-ecv-data-access-matrix/gcos-Land-ecv-above-ground-biomass%0D>
- [3] NASA, “The Water Cycle.” [Online]. Available: <https://smap.jpl.nasa.gov/resources/64/the-water-cycle-2/>
- [4] “GCOS Land ECV - Soil Moisture.” [Online]. Available: <https://www.ncdc.noaa.gov/gosic/gcos-essential-climate-variable-ecv-data-access-matrix/gcos-land-ecv-soil-moisture%0D>
- [5] W. N. Gov, “Responding to the Challenge of Climate and Environmental Change: NASA’s Plan for a Climate-Centric Architecture for Earth Observations and Applications from Space,” Tech. Rep., 2010. [Online]. Available: www.nasa.gov
- [6] D. Enrekhabi, S. Yueh, P. E. O’Neil, K. H. Kellogg, A. Allen, R. Bindlish, M. Brown, S. Chan, A. Colliander, W. T. Crow, N. Das, G. De Lannoy, R. S. Dunbar, W. N. Edelstein, J. K. Entin, V. Escobar, S. D. Goodman, T. J. Jackson, B. Jai, J. Johnson, E. Kim, S. Kim, J. Kimball, R. D. Koster, A. Leon, K. C. McDonald, M. Moghaddam, P. Mohammed, S. Moran, E. G. Njoku, J. R. Piepmeier, R. Reichie, F. Rogez, J. Shi, M. W. Spencer, S. W. Thurman, L. Tsang, J. Van Zyl, B. Weiss, and R. West, *SMAP Handbook Soil Moisture Active Passive Mapping Soil Moisture and Freeze/Thaw from Space*, 2014. [Online]. Available: http://smap.jpl.nasa.gov/system/internal/resources/details/original/178_SMAP_Handbook_FINAL_1_JULY_2014_Web.pdf
- [7] D. Entekhabi, E. G. Njoku, P. E. O’Neill, K. H. Kellogg, W. T. Crow, W. N. Edelstein, J. K. Entin, S. D. Goodman, T. J. Jackson, J. Johnson, J. Kimball, J. R. Piepmeier, R. D. Koster, N. Martin, K. C. McDonald, M. Moghaddam, S. Moran, R. Reichle, J. C. Shi, M. W. Spencer, S. W. Thurman, L. Tsang, and J. Van Zyl, “The soil moisture active passive (SMAP) mission,” *Proceedings of the IEEE*, 2010.
- [8] H. Carreno-Luengo, S. Lowe, C. Zuffada, S. Esterhuizen, and S. Oveisgharan, “Spaceborne GNSS-R from the SMAP mission: First assessment of polarimetric scatterometry over land and cryosphere,” *Remote Sensing*, vol. 9, no. 4, apr 2017.
- [9] R. Shah, J. L. Garrison, A. Egido, and G. Ruffini, “Bistatic Radar Measurements of Significant Wave Height Using Signals of Opportunity in L-, S-, and Ku-Bands,” *IEEE Transactions on Geoscience and Remote Sensing*, 2016.

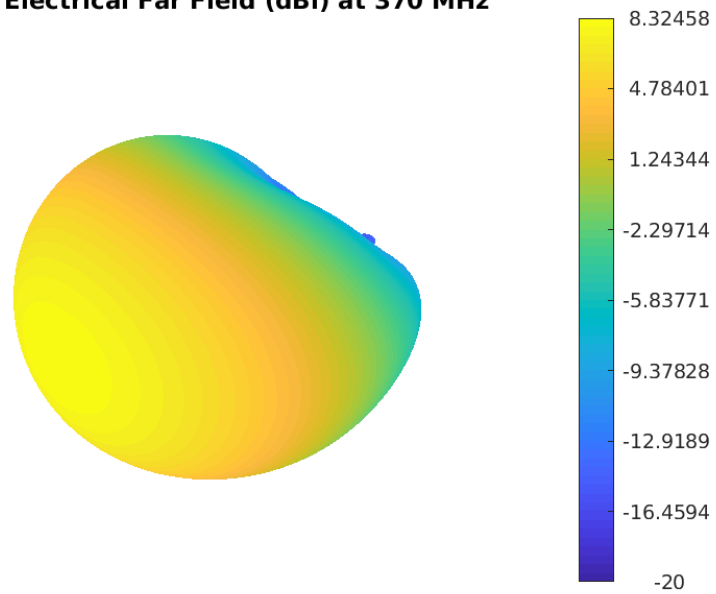
- [10] S. J. Katzberg and J. L. Garrison, "Utilizing GPS To Determine Ionospheric Delay Over the Ocean," 1996. [Online]. Available: <http://techreports.larc.nasa.gov/ltrs/ltrs.html>
- [11] R. Shah, J. L. Garrison, and M. S. Grant, "Demonstration of bistatic radar for ocean remote sensing using communication satellite signals," *IEEE Geoscience and Remote Sensing Letters*, 2012.
- [12] C. Chew, R. Shah, C. Zuffada, G. Hajj, D. Masters, and A. J. Mannucci, "Demonstrating soil moisture remote sensing with observations from the UK TechDemoSat-1 satellite mission," *Geophysical Research Letters*, 2016.
- [13] H. Kim and V. Lakshmi, "Use of Cyclone Global Navigation Satellite System (CyGNSS) Observations for Estimation of Soil Moisture."
- [14] D. Masters, P. Axelrad, and S. Katzberg, "Initial results of land-reflected GPS bistatic radar measurements in SMEX02," in *Remote Sensing of Environment*, 2004.
- [15] S. J. Katzberg, O. Torres, M. S. Grant, and D. Masters, "Utilizing calibrated GPS reflected signals to estimate soil reflectivity and dielectric constant: Results from SMEX02," *Remote Sensing of Environment*, vol. 100, no. 1, pp. 17–28, 2006.
- [16] J. L. Garrison, B. Nold, Y. C. Lin, G. Pignotti, J. R. Piepmeier, M. Vega, M. Fritts, C. Dutoit, and J. Knuble, "Recent results on soil moisture remote sensing using P-band signals of opportunity," in *Proceedings of the 2017 19th International Conference on Electromagnetics in Advanced Applications, ICEAA 2017*, 2017, pp. 1604–1607.
- [17] N. R. Peplinski, F. T. Ulaby, and M. C. Dobson, "Dielectric Properties of Soils in the 0.3–1.3-GHz Range," *IEEE Transactions on Geoscience and Remote Sensing*, vol. 33, no. 3, pp. 803–807, 1995.
- [18] T. Liebig. openEMS - Open Electromagnetic Field Solver. [Online]. Available: <https://www.openems.de>
- [19] D. M. Pozar, *Microwave engineering; 3rd ed.* Hoboken, NJ: Wiley, 2005. [Online]. Available: <https://cds.cern.ch/record/882338>
- [20] "Soil Moisture Experiment 2005 and Polarimetry Land Experiment (SMEX05/POLEX) Experiment Plan," Tech. Rep., 2005.
- [21] Stevens, "Soil Sensor  Users Manual," Tech. Rep., 2018.
- [22] IClimate, "iClimate." [Online]. Available: iClimate.org

APPENDICES

A. ANTENNA SIMULATIONS

The antenna was simulated using OpenEMS, a Finite-Difference Time-Differential method Electromagnetic wave simulator [18].

3D - Electrical Far Field (dBi) at 370 MHz



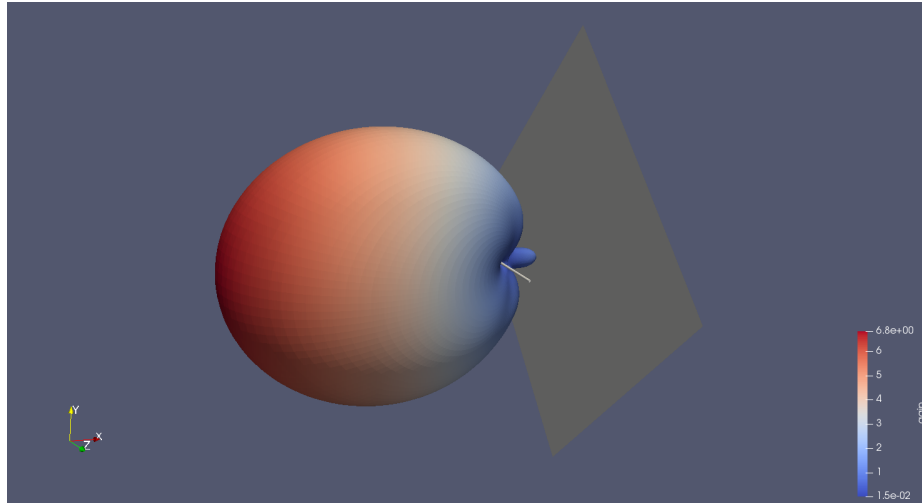


Fig. A.1.: Gain Pattern with Antenna and Backplane

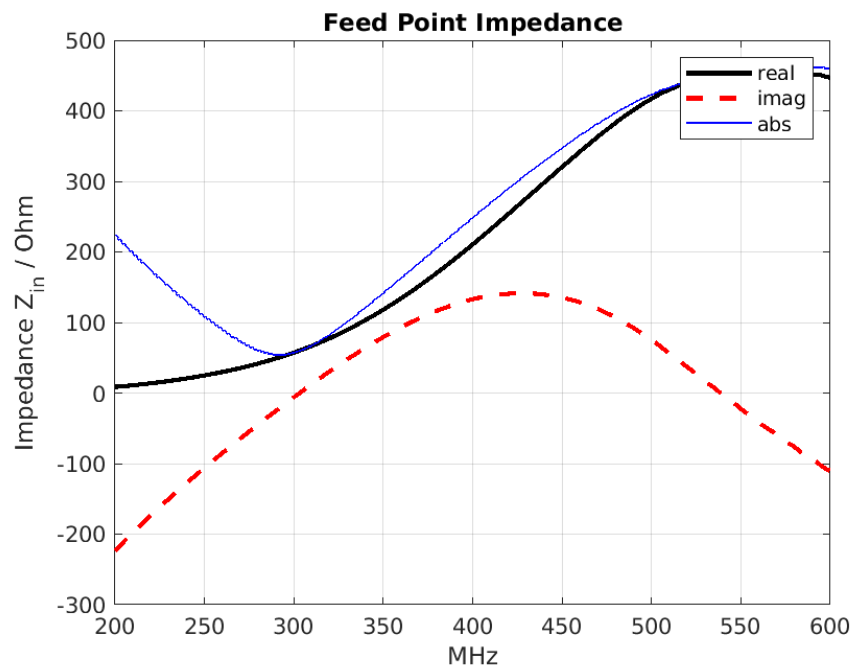


Fig. A.2.: Feed Impedance at 370Mhz: $150.9365 - 3.0728i \Omega$

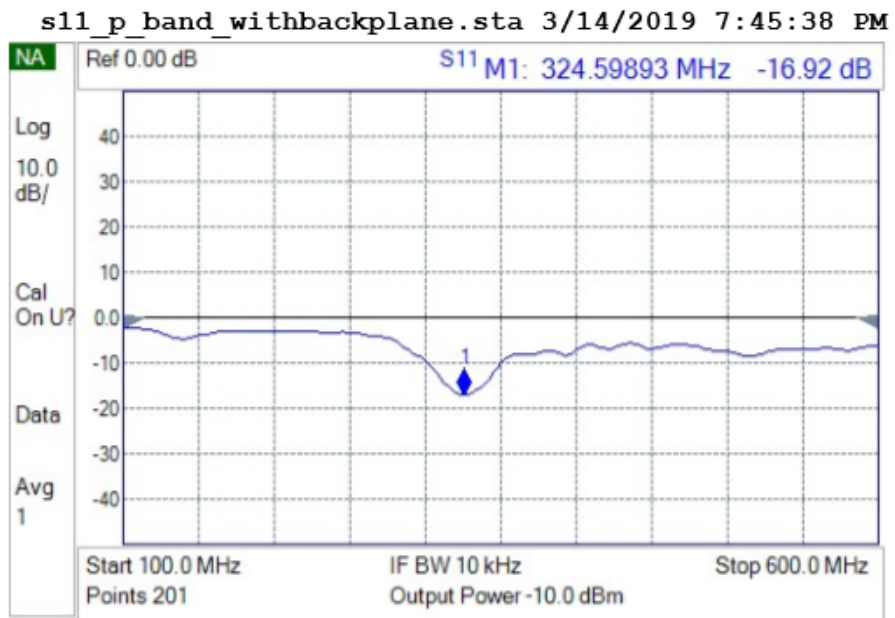
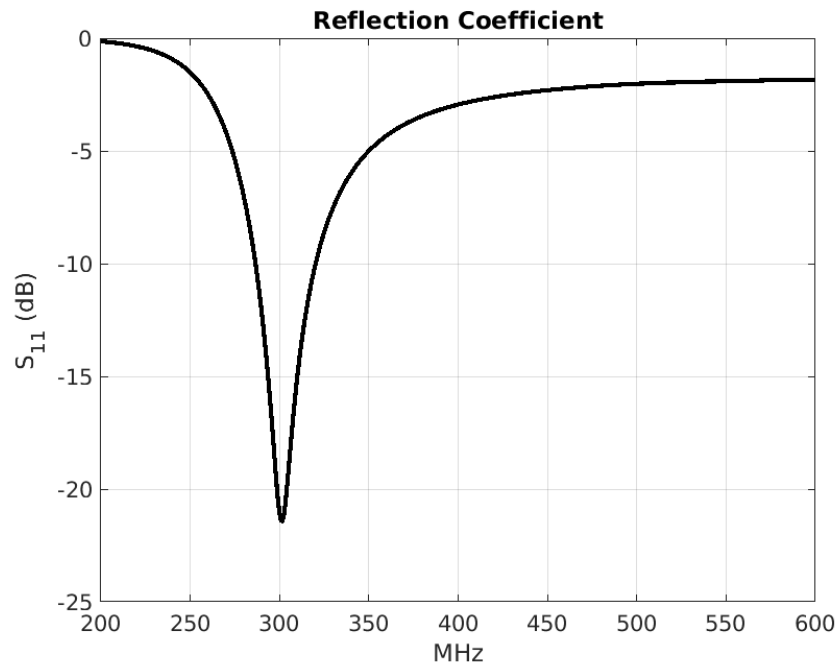


Fig. A.3.: Measured S_{11}

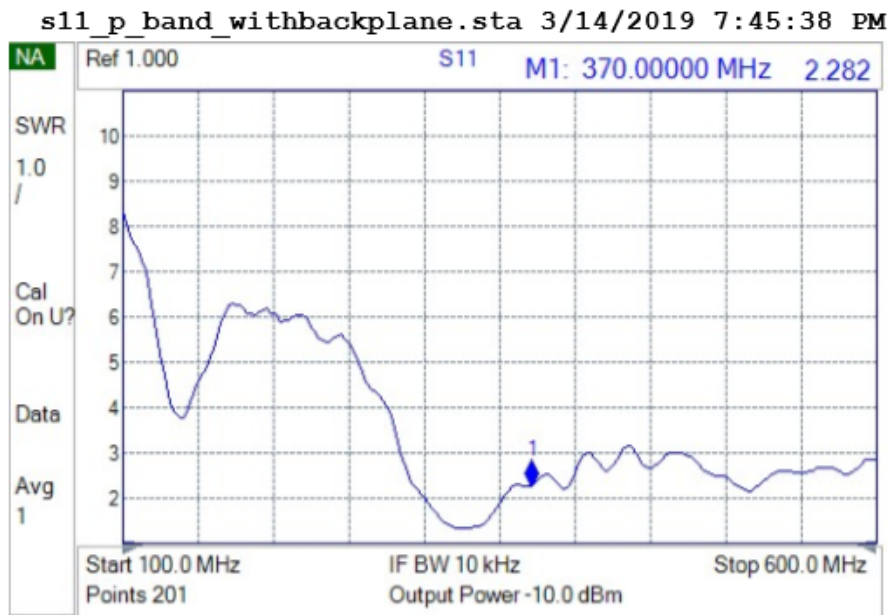
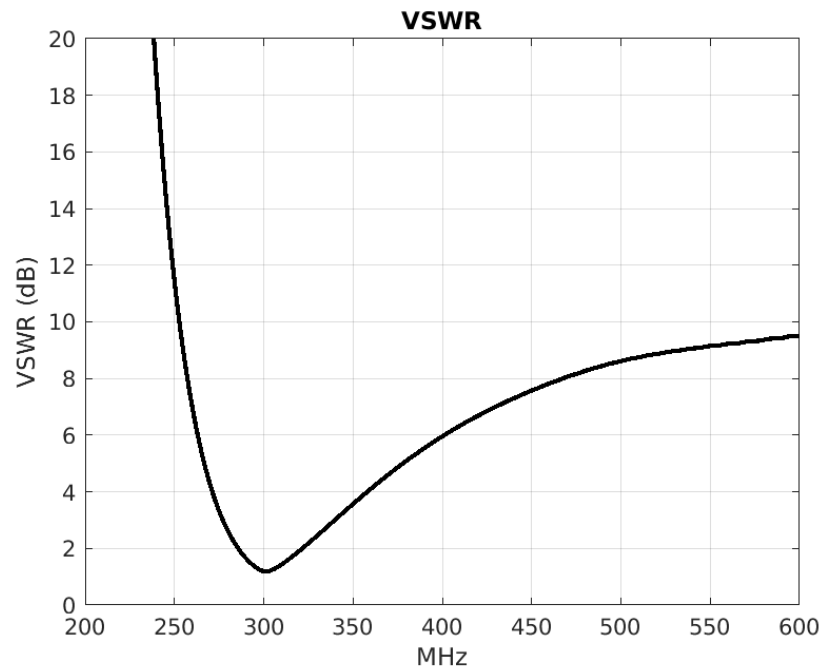
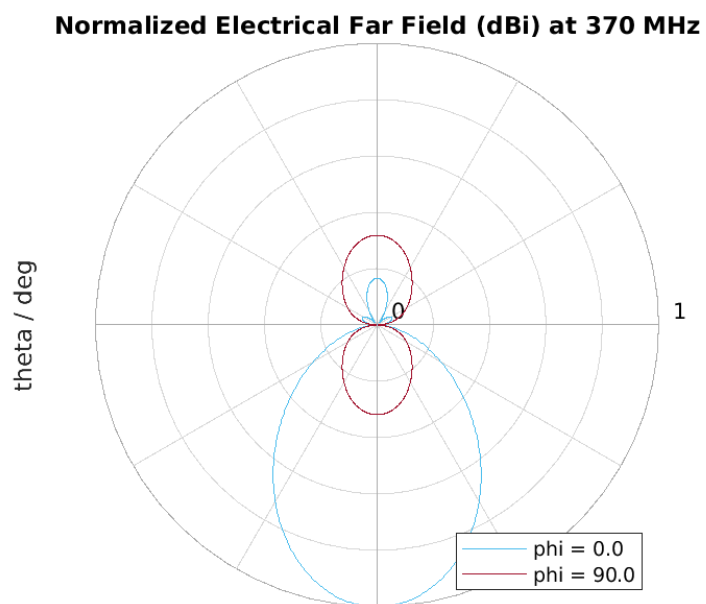
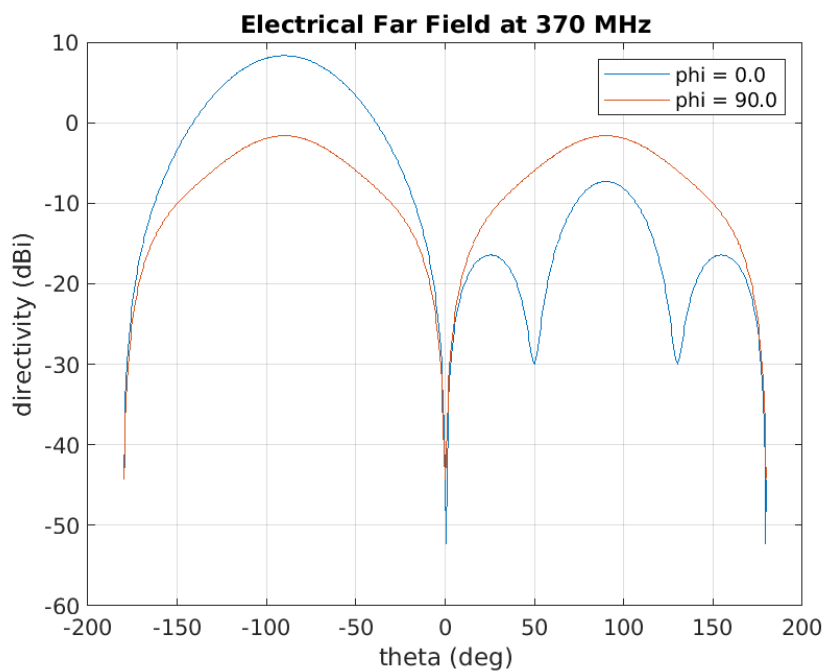


Fig. A.4.: Measured VSWR



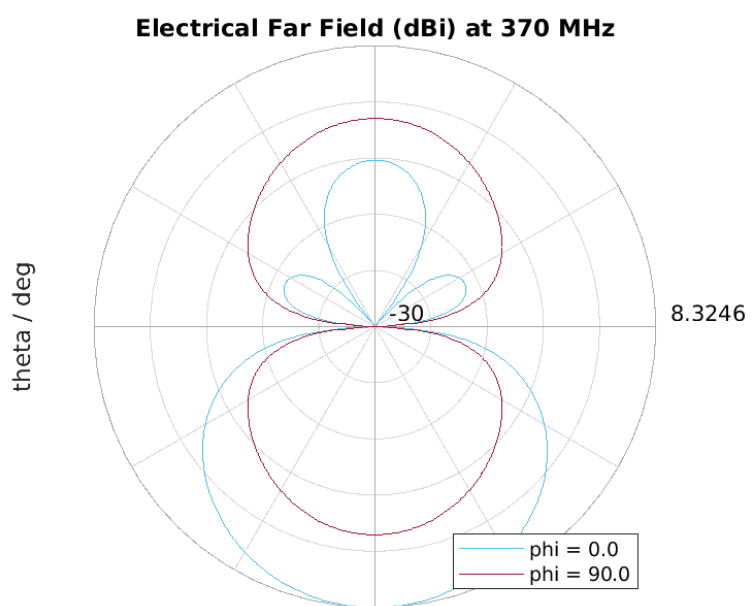




Fig. A.5.: Coax to Antenna Elements Soldering

P-Band Dipole Antenna – not to scale

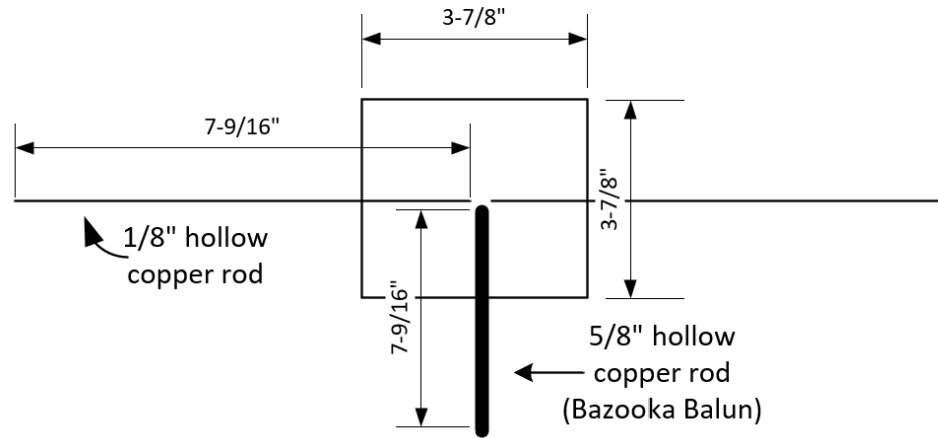


Fig. A.6.: P-Band Antenna Schematic

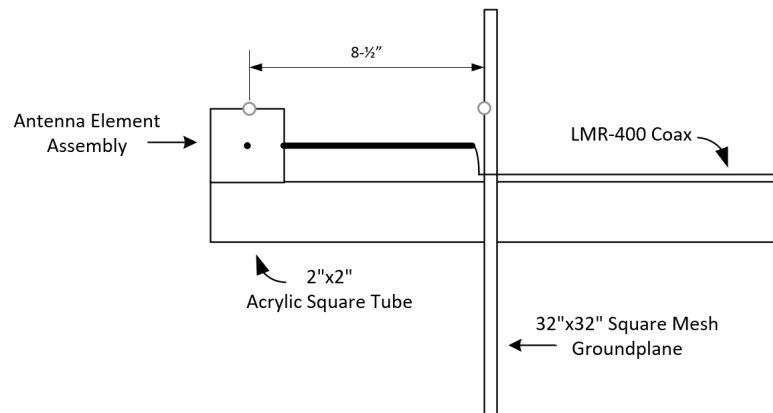


Fig. A.7.: P-Band Antenna Schematic

B. MICROWAVE SCHEMATICS

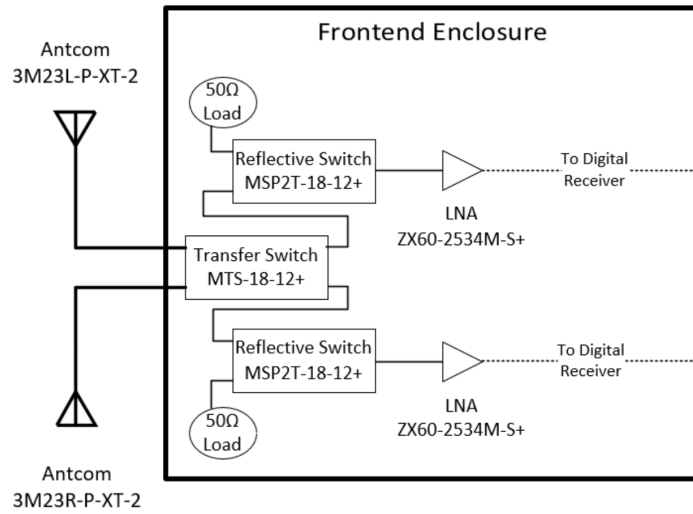


Fig. B.1.: 2017 S-Band Front End Block Schematic

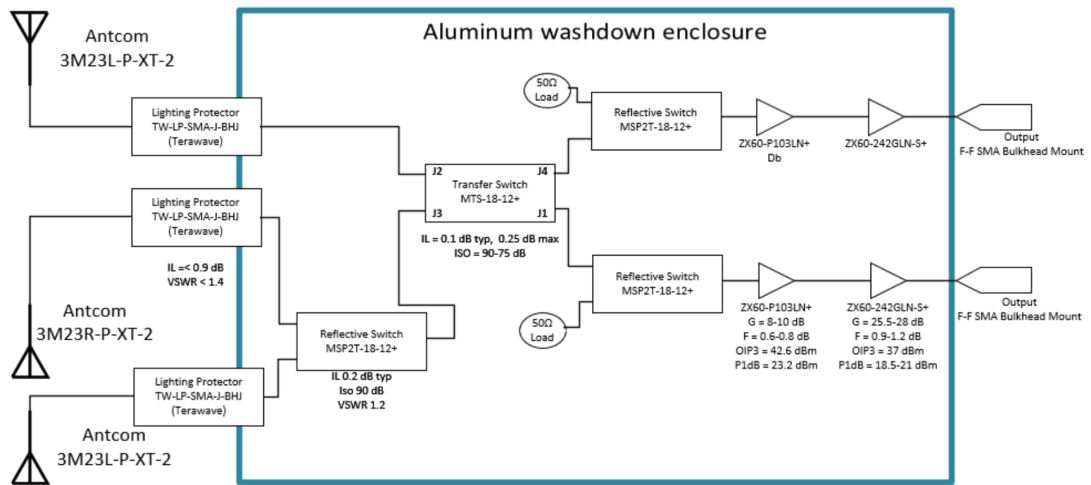


Fig. B.2.: 2018 S-Band Front End Block Schematic

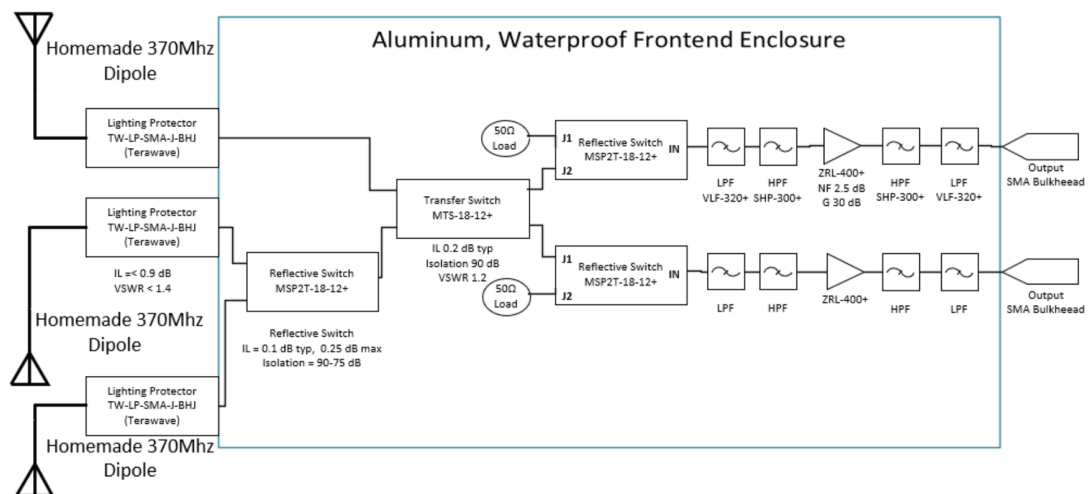


Fig. B.3.: 2018 P-Band Front End Block Schematic

Corn Sampling Sheet

Samples 3 plants at 3 locations.
SoOp Purdue Experiment 2018

Date _____ Samplers _____
 Weather _____ Note if there is any dew present _____
 Ground conditions _____

Row Spacing _____

Site ID	Rapid Scan NDVI	Height	# corn plants (per 1 m)	# of leaves	Stock circumference (bottom)	Bottom Leaf length above ground	Middle Leaf Length	# Cobs
Drainage Tile:								
Plant 2	-							
Plant 3	-							
Quarter Tile:								
Plant 2	-							
Plant 3	-							
Middle of Tile:								
Plant 2	-							
Plant 3	-							
R1								
R2								

For R1 and R2:

D. FRONT END 2017 SCATTERING PLOTS

These measurements were taken with a N9913A Field Fox portable network analyzer. Standard RG-58 SMA terminated coax were used for test cables. Measurements were not taken of the isolation between the direct and reflected channels due to the transfer switch. The 2017 front end was originally designed only to record one reflected signal polarization.

Network analyzer S measurements can be illustrated by figure D.1. S11 measurements only uses port 1, which transmits a wave and looks at the reflection. This is used for determining antenna resonance frequencies. S21 measurements transmit a wave from Port 1 and receives it on port 2. S21 measurements are used to determine the frequency response of the system in the following figures.

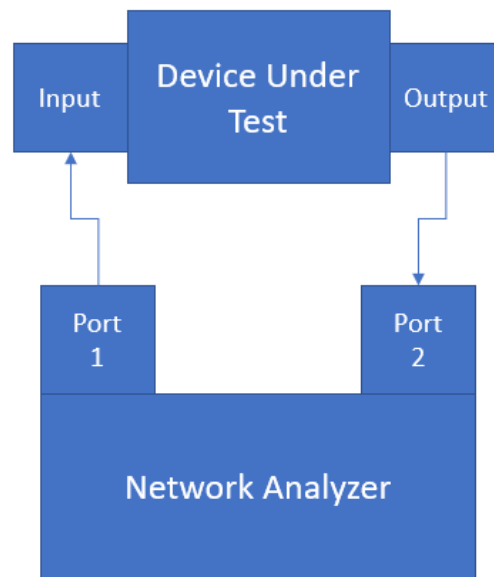
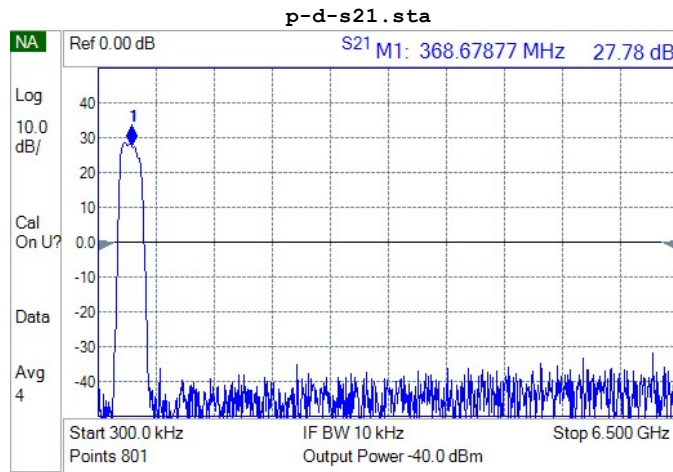
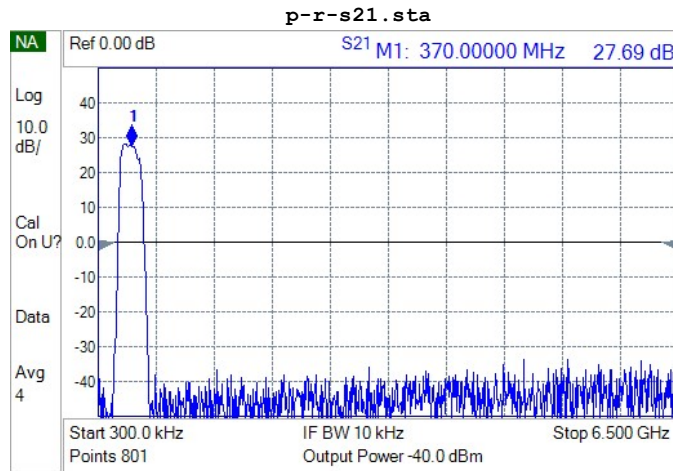


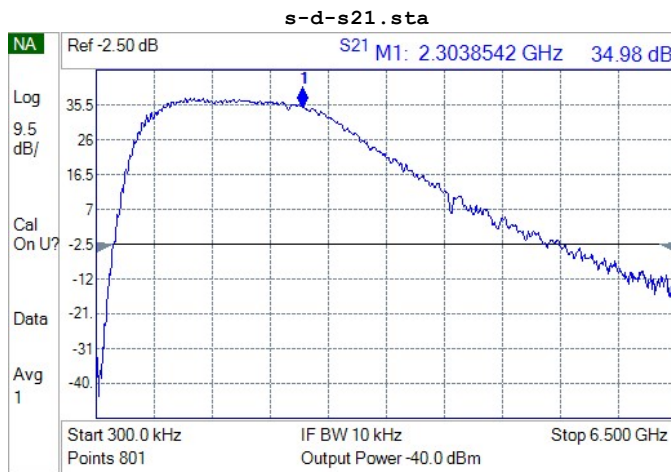
Fig. D.1.: Network Analyzer Graphic



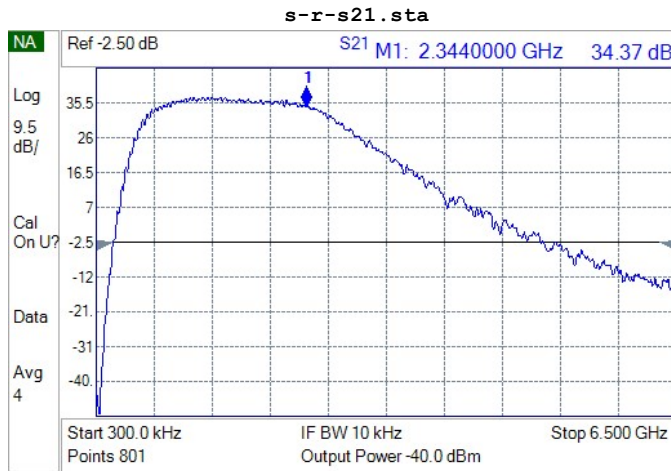
P-Band Direct Signal Path, S21



P-Band Reflected Signal Path, S21



S-Band Direct Signal Path, S21



S-Band Reflected Signal Path, S21

The following measurements were made of the 150 ft RG-8 cables connecting the front end to the equipment shed. The RG-8 cables were connected to the field fox network analyzer with short RG-58 leads, the network analyzer was calibrated to normalize out the RG-58 leads.

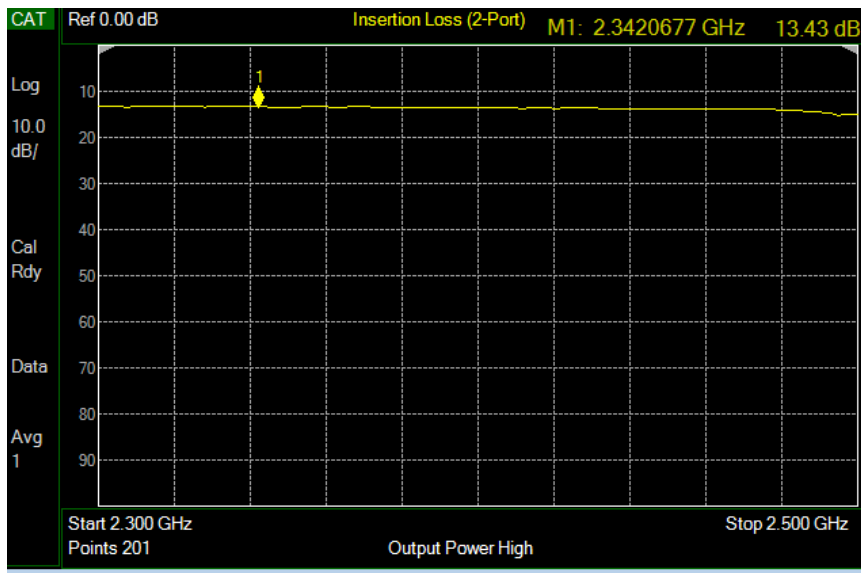


Fig. D.2.: S21, 150Ft RG-8 cable, S-Band range

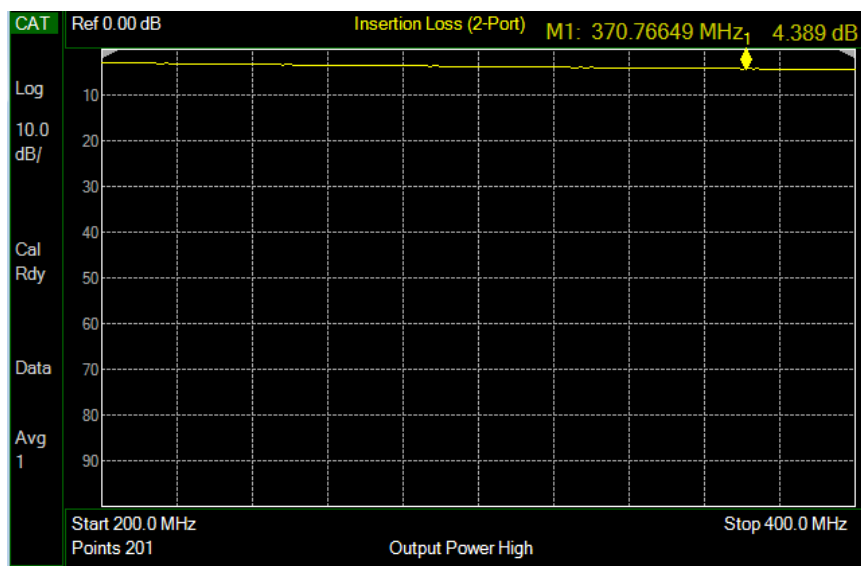


Fig. D.3.: S21, 150Ft RG-8 cable, P-Band range

E. FRONT END 2018 SCATTERING PLOTS

These measurements were taken with a N9918A Field Fox portable network analyzer. Rugged phase stable testing cables were used for the test cables. The network analyzer connections are shown in Figure D.1. The 2018 front end had implemented dual polarization for the reflected channel. See Figures B.2 and B.3 for the 2018 S and P Band front end schematics.

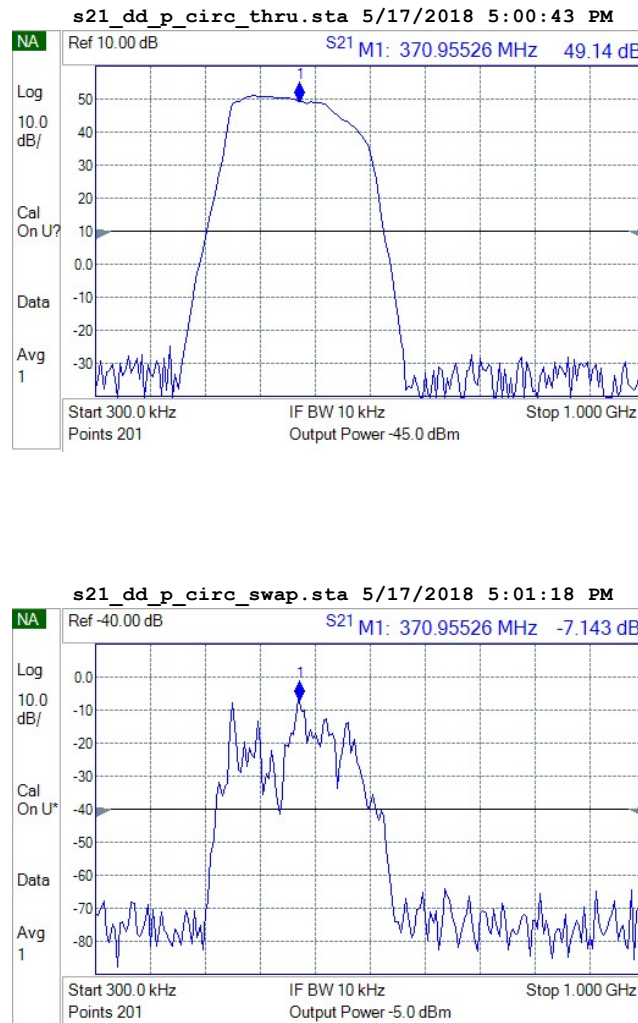


Fig. E.1.: P-Band S21 measurements

The upper figure is the “through” state, the lower figure is the swap state. The network analyzer is connected to the “direct” signal input for both plots. See Figure 2.8 for through state, Figure 2.9 for swap state. The swap state S21 plot is showing the isolation between the transfer switch channels.

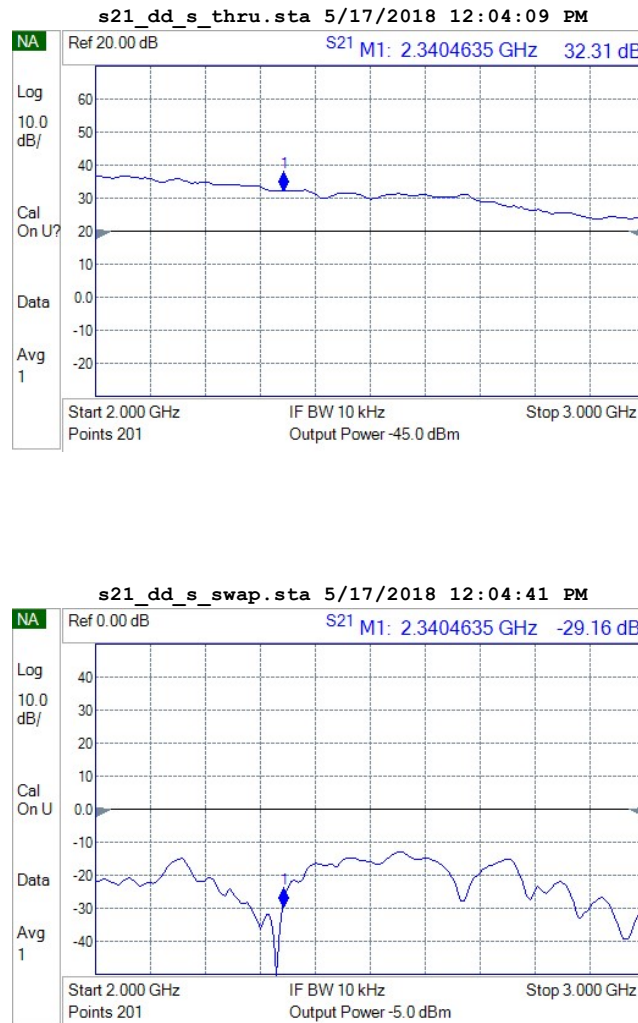


Fig. E.2.: 2018 S-Band S21 Plots

The upper figure is the "through" state, the lower figure is the swap state. The network analyzer is connected to the "direct" signal input for both plots. See Figure 2.8 for through state, Figure 2.9 for swap state. The swap state S21 plot is showing the isolation between the transfer switch channels.

F. FRONT END BILL OF MATERIAL

Item #	Quantity	Manufacturer	Model Number	Description
1	1	n.a.	20x16x10 in	Aluminum Washdown Enclosure
2	8	Terrawave	TW-LP-SMA-J-BHJ	Lighting Arrester
3	2	Milspec	MS3106A10SL	3 Pol Military Spec Circular Power Connector
4	1	Milspec	MS3102A18	4 Pol Military Spec Circular Power Connector
5	8	n.a.	n.a.	SMA Bulkhead adapter
6	1	Advantech	ADAM-4015	Datalogger
7	4	Mini-Circuits	ZRL0400+	P-Band Amplifier
8	3	Mini-Circuits	MTS-18-12B+	Transfer Switch
9	8	Mini-Circuits	MSP2T-18-12+	Reflective Switch
10	3	Omega	SA1-RTD	Omega Temp Sensors
11	1	n.a.	n.a.	Custom Capacitor Bank for Voltage Smoothing
12	4	Mini-Circuits	ZX60-P103LN+	Pre-Amplifier
13	2	Mini-Circuits	ZX60-2534M-S+	S-Band Amplifier 2017
14	2	Mini-Circuits	ZX60-242GLN-S+	S-Band Amplifier 2018
15	2	Mini-Circuits	VLF-320+	Low Pass P-Band Filter
16	2	Mini-Circuits	SHP-300+	High Pass P-Band Filter

Table F.1.: Phase Calibration Bill of Material

Item #	Quantity	Manufacturer	Model Number	Description
1	1	Mini-Circuits	ZAPD-2-272-S+	S-Band Power Splitter
2	2	Mini-Circuits	Z99SC-62-S+	P-Band Power Splitter
3	1	Generic	Generic	GPIO Driven Relay Model, 4 relays
4	1	Raspberry Pi Foundation	Model 2 B	Raspberry Pi
5	1	USB Power Supply	Generic	Power Supply for Raspberry Pi
7	3	Mini-Circuits	MSP2T-18-12+	Reflective Switches

Table F.2.: Phase Calibration Bill of Material